



**Calhoun: The NPS Institutional Archive**  
**DSpace Repository**

---

Theses and Dissertations

1. Thesis and Dissertation Collection, all items

---

1988

# The residual strength of a ship after an internal explosion

Surko, Stephen William

Monterey California. Naval Postgraduate School

---

<http://hdl.handle.net/10945/23106>

---

This publication is a work of the U.S. Government as defined in Title 17, United States Code, Section 101. Copyright protection is not available for this work in the United States.

*Downloaded from NPS Archive: Calhoun*



Calhoun is the Naval Postgraduate School's public access digital repository for research materials and institutional publications created by the NPS community. Calhoun is named for Professor of Mathematics Guy K. Calhoun, NPS's first appointed -- and published -- scholarly author.

**Dudley Knox Library / Naval Postgraduate School**  
**411 Dyer Road / 1 University Circle**  
**Monterey, California USA 93943**

<http://www.nps.edu/library>













10  
10  
10



DEPARTMENT OF OCEAN ENGINEERING

MASSACHUSETTS INSTITUTE OF TECHNOLOGY

CAMBRIDGE, MASSACHUSETTS 02139

---

THE RESIDUAL STRENGTH OF A SHIP

AFTER AN INTERNAL EXPLOSION

by

STEPHEN WILLIAM SURKO

LT, USN ' ' '

COURSE XIII-A

JUNE 1988

- NPGS COPY -

THESIS  
57641

T239260





THE RESIDUAL STRENGTH OF A SHIP  
AFTER AN INTERNAL EXPLOSION

by

STEPHEN WILLIAM SURKO

B.S. Ocean Eng., United States Naval Academy  
(1982)

Submitted to the Department of  
Ocean Engineering  
in Partial Fulfillment of the  
Requirements for the Degrees of

MASTER OF SCIENCE IN NAVAL ARCHITECTURE  
AND MARINE ENGINEERING

and

MASTER OF SCIENCE IN MECHANICAL ENGINEERING

at the

MASSACHUSETTS INSTITUTE OF TECHNOLOGY

May 1988

© Massachusetts Institute of Technology 1988





THE RESIDUAL STRENGTH OF A SHIP  
AFTER AN INTERNAL EXPLOSION

by

STEPHEN WILLIAM SURKO

Submitted to the Department of Ocean Engineering  
in partial fulfillment of the requirements  
for the degrees of Master of Science in  
Naval Architecture and Marine Engineering  
and Mechanical Engineering

ABSTRACT

An internal airblast from a missile explosion produces tearing, holing, and dishing of a ships' structural plating.

In order to analyze the residual strength of a ship after an internal explosion, a typical ship compartment was considered to be composed of flat square plates subjected to uniaxial compression, and the damage effects were examined independently. The holing was considered to be a centrally located circle. Plastic limit load analysis of a flat plate indicates that ultimate strength decreases in proportion to increasing hole size. Elastic-plastic analysis indicates that ultimate strength is little affected by hole size until the holing reaches half the plate width, and is essentially equal to the ultimate load described by the effective width concept. An extension of the concept of small imperfections to dished plates suggests that the ultimate strength is reduced by roughly 10 percent from that of a flat plate. The extensional collapse mode analysis describes folding and strength beyond peak load. Fully plastic crack propagation was examined, but its limiting effect can not be precisely described.

A small program of experimentation was developed to gain qualitative insights into the interaction and cumulative effect of the various damage modes. Seven mild steel boxes were constructed of four square side plates with length-to-thickness ratios of 90 and two stiffened end plates to model different damage effects. The experimental results indicate that the plastic limit load does not define the peak load of slender plates. Increased hole size appears to decrease ultimate strength gradually. Dishing on the order of 5 to 15 plate thicknesses reduces ultimate strength by roughly 15 to 35 percent. The mean crushing load allows damaged structural plating to continue to support loading on the order of 5 to 10 percent of the tensile yield load. Although crack growth was not a factor during testing, it could be important in shipboard structural plating which is relatively thinner and harder than the tested specimens.

THESIS SUPERVISOR: Tomasz Wierzbicki, Professor of Applied Mechanics

THESIS ADVISOR: Frank McClintock, Professor of Mechanical Engineering



FOR LIDDY





## ACKNOWLEDGEMENTS

It is a pleasure to thank those who have given me guidance, insight, and support throughout my research and the writing of this thesis. Professor T. Wierzbicki encouraged me to pursue my interest in the topic of warship survivability, and his untiring guidance and wisdom enabled me to successfully grapple with such a complex subject. Professor F.A. McClintock provided insight as I examined the subject of fully plastic fracture, and aided me in my experimentation. Mr. M. Said and E. Kadala of the Naval Sea Systems Command provided much appreciated interest and information on battle damage effects and warship design. The Office of Naval Research provided the funding required for experimentation. I would especially like to thank my parents and my fiancée for their unfailing love and support throughout it all.





## TABLE OF CONTENTS

LIST OF FIGURES .....	7
LIST OF TABLES .....	9
NOTATION .....	10
 1. <u>INTRODUCTION</u> .....	 12
1.1 THE ANTISHIP MISSILE THREAT .....	12
1.2 MODERN U.S. NAVY WARSHIP DESIGN .....	14
1.3 LOCAL DAMAGE EFFECTS AND METHODS OF ANALYSIS .....	15
 2. <u>PLASTIC LIMIT LOAD OF A FLAT PLATE</u> .....	 20
2.1 INTRODUCTION .....	20
2.2 PHYSICAL BASIS OF PLASTICITY .....	20
2.3 LIMIT LOAD ANALYSIS .....	21
2.4 PLASTIC LIMIT LOAD OF A HOLED PLATE .....	23
 3. <u>ELASTIC-PLASTIC BUCKLING AND POST-BUCKLING ANALYSIS</u> .....	 30
3.1 INTRODUCTION .....	30
3.2 EFFECTIVE WIDTH CONCEPT .....	30
3.3 BUCKLING AND POST-BUCKLING ANALYSIS .....	32
3.4 ULTIMATE STRENGTH OF A HOLED PLATE .....	34
3.5 COMPARISON WITH EXPERIMENTAL RESULTS .....	37
 4. <u>DISHING OF PLATES UNDER IMPULSIVE LOADING</u> .....	 44
4.1 INTRODUCTION .....	44
4.2 DYNAMIC EFFECTS OF AN INTERNAL AIRBLAST .....	45
4.3 MEMBRANE MODE FINITE ELEMENT ANALYSIS .....	46
4.4 EXPERIMENTAL RESULTS AND EMPIRICAL ANALYSIS .....	48
 5. <u>STRENGTH OF A DISHED PLATE</u> .....	 56
5.1 INTRODUCTION .....	56
5.2 PHYSICAL BASIS OF DEFORMATION MECHANISMS .....	56
5.3 LARGE INITIAL IMPERFECTION ANALYSIS .....	58
5.4 EXTENSIONAL COLLAPSE MODE ANALYSIS .....	60



5.5	COMPARISON WITH EXPERIMENTAL RESULTS .....	65
6.	<u>MIXED MODE CRACK PROPAGATION</u> .....	72
6.1	INTRODUCTION .....	72
6.2	PHYSICAL BASIS OF PLASTIC FRACTURE .....	73
6.3	ANALYTIC APPROACHES TO PLASTIC FRACTURE .....	74
6.4	RIGID-PLASTIC FRACTURE ANALYSIS .....	76
6.5	PLASTIC LIMIT LOAD FRACTURE ANALYSIS .....	78
6.6	CRACK PROPAGATION FROM A CIRCULAR HOLE .....	81
7.	<u>EXPERIMENTS AND DISCUSSION</u> .....	84
7.1	INTRODUCTION .....	84
7.2	CUMULATIVE STRUCTURAL EFFECT OF DAMAGE .....	84
7.3	EXPERIMENTAL METHOD .....	85
7.4	EXPERIMENTAL RESULTS .....	90
7.5	DISCUSSION OF RESULTS .....	91
7.6	RESIDUAL STRENGTH OF A WARSHIP AFTER AN INTERNAL EXPLOSION .....	96
8.	<u>CONCLUSION</u> .....	103
8.1	IDEAS FOR CONTINUED RESEARCH .....	104
	REFERENCES .....	105
APPENDICES		
A	Load Versus Displacement Experimental Data for Crushing of Specimens .....	110





## LIST OF FIGURES

Figure 1.1	Categorization of naval antiship weapons	18
Figure 1.2	Diagram of battle damage to USS <u>Brownson</u> (DD-518) which sank due to loss of structural integrity	18
Figure 1.3	Summary of battle damage to several World War Two U.S. destroyers which sank due to loss of structural integrity	19
Figure 1.4	Analysis of battle damage	19
Figure 2.1	Graph of typical stress vs. strain for mild steel	27
Figure 2.2	Square plate with a circular hole	27
Figure 2.3	Discontinuous stress field of square plate with a central circular hole (uniform traction)	28
Figure 2.4	Graph of bounds for a square plate with a central circular hole using Tresca criterion	28
Figure 2.5	Graph of uniform traction bounds for a square plate with a central circular hole using Mises criterion	29
Figure 2.6	Stress and displacement fields for a square plate with a central circular hole (uniform displacement)	29
Figure 3.1	Real stress distribution and effective plate width due to in-plane compressive loading	40
Figure 3.2	Graph of theoretical buckling loads vs. cutout ratio for square plates	40
Figure 3.3	Buckled form and critical values of axial stress for simply supported plates subjected to in-plane compressive loading	41
Figure 3.4	Assumed stress distribution across holed plate	41
Figure 3.5	Graph of effective width vs. maximum stress for various cutout ratios	42
Figure 3.6	Graph of theoretical analysis and experimental results for ultimate load vs. cutout ratio for square and rectangular plates	42
Figure 3.7	Graph of theoretical analysis and experimental results for uniform traction (constant stress) buckling load vs. cutout ratio for a square plate	43
Figure 3.8	Graph of theoretical analysis and experimental results for uniform displacement (constant strain) buckling load vs. cutout ratio for a square plate	43
Figure 4.1	Graph of pressure vs. time response recorded at a point on the wall of a partially closed chamber following an internal explosion	53
Figure 4.2	Analytic model showing discretization of a square plate	53
Figure 4.3	Final mode profile and contour plot of a typical explosive test for a square plate	54
Figure 4.4	Graph of analytic solutions and experimental results for deflection-to-thickness ratio vs. impulse for circular plates	54
Figure 4.5	Graph of analytic solutions and experimental results for deflection-to-thickness ratio vs. impulse for square plates	55



Figure 4.6	Graph of deflection-to-thickness ratio vs. dimensionless damage number $\theta_q$ for quadrangular plates	55
Figure 5.1	Graphs of theoretical ultimate load vs. strain for square plates with different slenderness values	67
Figure 5.2	Graph of theoretical ultimate load vs. slenderness for square constrained plates with different initial deflections	67
Figure 5.3	Graph of theoretical analysis and experimental results for ultimate load vs. slenderness for square plates including the effects of initial deflections	68
Figure 5.4	Typical structural elements	68
Figure 5.5	Basic folding mode of a L-shaped angle element with a continuous and smooth displacement field	69
Figure 5.6	Plastic distortion of a rectangle into a trapezoid	69
Figure 5.7	Photograph of partially crushed cruciform	70
Figure 5.8	Graph of typical load vs. deflection characteristics of a crushed cruciform	70
Figure 5.9	Cruciform with holed half-plates	71
Figure 5.10	Graph of theoretical analysis and experimental results for mean crushing strength vs. half-plate length-to-thickness ratio	71
Figure 6.1	The three modes of loading which lead to crack growth	82
Figure 6.2	Axial splitting of ductile metal tube	82
Figure 6.3	Quadrant of damaged plate and assumed displacement fields	83
Figure 6.6	Graph of upper bound limit load vs. displacement ratio for different initial angles of flare (dishing)	83
Figure 7.1	Summary of damage effect failure modes for shipboard structural plating with a length-to-thickness ratio of 250	98
Figure 7.2	Specimen types with different simplified dishing (lateral deflection) modes	98
Figure 7.3	Photograph of testing apparatus	99
Figure 7.4	Graph of load vs. deflection for baseline and Type A (Accordion bulge) specimens	99
Figure 7.5	Graph of load vs. deflection for baseline and Type B (Basketball bulge) specimens	100
Figure 7.6	Photograph of specimen B1 shortly after ultimate load was reached	100
Figure 7.7	Photograph of specimen A2 shortly after ultimate load was reached	101
Figure 7.8	Photograph of tearing from a starter crack in specimen A2	101
Figure 7.9	Summary of damage effect failure modes and experimental results for specimen side plates with a length-to-thickness ratio of 90	102
Figure 7.10	Graph of plate buckling coefficient vs. aspect ratio for different boundary conditions	102





## LIST OF TABLES

Table 4.1	Typical Johnson's number damage regime (mild steel at room temperature impacted by a projectile)	50
Table 5.1	Empirical relationships to describe the effect of small initial imperfections upon effective plate width	58
Table 7.1	Tensile properties of ASTM A-515 grade 70 mild steel and ASTM A-710 grade A - class 1 low-carbon steel	87
Table 7.2	Initial structural condition for all specimens	89
Table 7.3	Ultimate and mean crushing load experimental results for all specimens	91



## NOTATION

Most notation will be specifically defined where it is first introduced. The following table will serve as a reference guide. Where more than one meaning has been assigned to a symbol, the correct use will be obvious from the text or explicitly defined.

A	Cross-sectional area, crack area
a	Length of plate
b	Width of plate
$b_e, b_{ec}$	Effective width of unperforated plate, corrected effective width for holed plate
$C_r$	Coefficient of deflection function
c	Diameter of hole
$c_t$	Width of tensile region in unperforated plate
D	Plate flexural rigidity = $Et^3 / [12(1 - \nu^2)]$
	Material constant
E	Young's modulus
F	Airy stress function
H	Half-width of the folding zone
	Kinetic energy
h	Plate thickness
I	Impulse
K	Plate buckling coefficient
m	Wavelength parameter
$N_x, N_y, N_{xy}$	Stress resultants (membrane)
n	Material constant
$\bar{n}$	Unit stress resultants
P	Load
$P_{crit}$	Critical load of unperforated plate
$P_h$	Compressive load removed by hole
$P_m$	Mean crushing load
$P_y$	Tensile yield load (squash load)
Q, q	Generalized stress, strain
R	Fracture toughness (essential work of fracture)
r	Coordinate, radius of circular plate & tube



$t$	Time
$U, U_b, U_m$	Strain energy (bending, membrane)
$u, v, w$	Displacements
$V$	Volume
$v$	Velocity
$W, W^p, W^c$	Work (plastic, crack propagation)
$w_c, w_{cf}$	Central deflection, final central deflection
$x, y, z$	Structural coordinates
$Y$	Flow strength
$\alpha$	Johnson's damage number
$\beta$	Slenderness ratio
$\epsilon$	Extensional strain
$\epsilon_{xx}, \epsilon_{yy}, \epsilon_{xy}$	Plane strain components
$\epsilon_\theta$	Average hoop strain
$\bar{\epsilon}$	Effective strain
$\Gamma$	Total plastic work per unit volume
$\phi$	Edge displacement parameter, deflection modeshape
$\Lambda, \Lambda_r$	Elastic strain energy (residual)
$\lambda_p$	Reference slenderness for plate buckling
$\nu$	Poisson's ratio
$\rho$	Material density
$\sigma$	Normal stress
$\sigma_{xx}, \sigma_{yy}, \sigma_{xy}$	Plane stress components
$\sigma_{crit}$	Critical stress
$\sigma_o$	Flow stress (damage stress)
$\sigma_Y$	Yield strength
$\bar{\sigma}$	Effective stress
$\theta, \theta_c, \theta_q$	Modified damage number, circular & quadrangular plates
$\xi$	Distance parameter
$\nabla^4$	$= \partial^4( ) / \partial x^4 + 2 \partial^4( ) / \partial x^2 \partial y^2 + \partial^4( ) / \partial y^4$





## 1. INTRODUCTION

### 1.1 The Antiship Missile Threat

Modern naval warships must be built to survive and operate in a multiple hostile threat environment. In addition to facing heavy seas and storms, a warship may be subjected to attack by a variety of weapons such as torpedoes, mines, gunfire, bombs, and missiles (Figure 1.1). Some of the more common and lethal weapons are antiship missiles equipped with semi-armor piercing warheads with small, high explosive (HE) payloads. Such antiship missiles first penetrate a ship's outer structure and then, by a delayed-fuze mechanism, detonate within the confines of the superstructure or hull to cause damage to the structure and internal systems [1]. The purpose of this paper is to analyze the structural ability of a destroyer-sized warship to withstand the effect of explosive loading associated with a missile attack.

The various antiship missiles produced by different nations all have similar components. A typical antiship missile has a propulsion section (multi-stage solid fuel and/or a turbojet engine plus a booster for surface/submarine launch), fuel tank, guidance system, and a warhead enclosed in an aerodynamic cylinder. Small antiship missiles are widely produced and exported throughout the world. Their sizes range from the now infamous 17 foot French EXOCET with a 200 pound warhead down to the 10 foot Norwegian PENGUIN with a 264 pound warhead. Most antiship missiles attack their targets with a sea skimming trajectory which make them difficult to detect and track.

Modern antiship missiles' blast and fragmentation warheads are little more sophisticated than the free-fall bombs used against ships



since the start of World War Two. The effect of aerial bombs and kamikaze aircraft attacks on destroyers during World War Two illustrates the type and extent of damage produced by such weapons. A direct hit of an aerial bomb causes damage to the above-water and underwater sections of the hull (sometimes with a breakoff of an extremity), fragmentation damage to exposed stations and superstructures, flooding of compartments producing a change in draft, and the outbreak of fires. The main propulsion spaces, electrical equipment, and the ship guns could be put out of action as a result of a high explosive's blast and fragmentation damage. Aerial bomb explosions put destroyers out of action basically because of damage to guns and technical equipment (about 50 percent of the cases, of which almost 25 percent were due to shock vibrations) and because of loss of watertight integrity (35 percent). Fires and explosions and destruction of the overall strength of the hull of the ship had less significance. The explosive action of kamikaze aircraft most often caused destroyers to lose mission capability rather than to sink [2]. Of 30 U.S. destroyers sunk during World War Two due to gunfire, bomb or kamikaze attack, only six resulted from loss of structural integrity of the hull (Figures 1.2, 1.3) [3].

Significant ship structural damage due to weapons effects has been scant since World War Two and has generally not been as well documented [3]. During the recent Falklands Conflict, however, the British Royal Navy faced a multiple hostile threat environment. HMS Ardent, a 3250 ton frigate suffered four aerial bomb hits before it was "mission killed" and required three more hits before it sank. HMS Antelope, sister ship of HMS Ardent, sank after one 500 lb. bomb exploded and started an uncontrollable fire that caused several secondary explosions.



HMS Sheffield was hit by an EXOCET antiship missile which failed to explode, but which penetrated and ignited the ship's main fuel supply tank with its still burning rocket fuel. The ensuing fire and smoke was uncontrollable. The 15,000 ton roll-on/roll-off container ship Atlantic Conveyor was also lost due to a single EXOCET missile hit which produced uncontrollable fires [4].

## 1.2 Modern U.S. Navy Warship Design

United States warship structures have always been implicitly designed with survivability in mind. Incorporating lessons learned from World War Two into such design practice as crack arrestors, requiring gradual transitions, using continuous welds, providing hull girders with a 1.0 ton per square inch reserve primary strength and limiting design primary stress throughout the structure, has produced more survivable warship designs. David W. Taylor Research and Development Center has been developing material fracture control technology. Strict fabrication requirements minimize the deleterious effects of poor structural detailing, failed welds, stress concentrations, etc. in high intensity dynamic pressure environments and also contribute to the survivability of the warship [3]. Current techniques for predicting weapon effects on structures are, however, limited. To simplify the determination of residual strength after an attack, the Naval Sea Systems Command considers all damaged structure to be "ineffective" [3].

Small, unarmored, warships such as destroyers are likely to suffer local structural failure from the initial explosion and be faced with spreading fire causing further damage and secondary explosions. The large amount of flammable material on modern warships make them more





susceptible to fire damage than World War Two warships. One of the lessons learned from the Falklands Conflict, and further emphasized in the Persian Gulf, was that aluminum structures failed because of the intense heat produced by fires. Although steel structures may be weakened or distorted by shipboard fires on the order of 1800°F to 2000°F, aluminum structures will rapidly sag and melt at such temperatures [5]. Since World War Two, small warships were built with aluminum superstructures to reduce topside weight and associated costs. The U. S. Navy's new DDG-51 Arleigh Burke Class destroyer incorporates improved design practices, all steel construction, and damage control features such as shock mounted and blast hardened structures and equipment along with redundant firefighting capabilities. Such warships can undoubtedly survive the secondary effects of missile damage better than the the destroyers of World War Two or the British warships in the Falklands Conflict.

Contemporary tactical doctrine calls for coordinated saturation attacks by antiship missiles to overcome a warship's active defenses and ensure several missile hits [4]. Even with severe battle damage, a hardened structure provides a warship with a "keep afloat" capability. To improve this passive defense capability against the growing antiship missile threat it is important to understand how a warship's structural plating is affected by the damage produced by an internal explosion. The capacity of a warship's structure to absorb and contain missile hits is vital to its ability to survive and operate in a hostile environment.

### 1.3 Local Damage Effects and Method of Analysis

An internal airblast from a missile explosion imparts reverberating



high-intensity pressure pulses against ship structural plating. The HE detonation produces gasses with a temperature on the order of 5500°F and pressure reaching 750,000 psi. The total impulse is a function of missile momentum and explosive energy. After passage and decay of the initial shock wave, confinement of the explosion gases leads to a pressure loading with a typical duration on the order of several seconds [6].

Structural damage is caused by a combination of (1) holing of internal structural plating, (2) blast overpressure within confined spaces, (3) fragments from warhead break-up, (4) fragmentation/spalling of interior bulkheads and decks, and (5) fire [1]. These modes of failure interact and may cause structural collapse of a local or global character. The effect of fragmentation on structural integrity is generally insignificant and is not evaluated. The subsequent effect of heat and fires produced by missile damage on structural integrity has been analyzed by Hiddemen [7]. The structural effects of supporting stiffeners (girders, beams, etc.) have been examined by Faulkner [8] and others. This paper is specifically concerned with the residual strength in a ship's structural plating which has suffered an internal airblast.

The dynamic interaction of damage effects within a complex ship structure is not well understood. In order to analyze this situation, a typical warship compartment structure is considered to be composed of flat square plates subjected to quasi-static uniaxial loading, and the damage effects are examined independently. Structural damage consists of some combination of tearing, holing, and deflection.

The extent of holing caused by the missile explosion is based upon U.S. Navy experiences [1]. Holing is caused by the high



velocity gradients across the plate surface (due to localized pressure loading) [6]. Roberts and Azizian [9] have shown analytically and experimentally that hole shape has little effect on structural strength. As a reasonable simplification, therefore, the holing is considered to be a centrally located circle.

As an initial approximation of residual strength after damage, a plastic limit load analysis and elastic-plastic buckling analysis are developed for a flat plate with a circular hole. The dishing of a flat plate under impulsive loading is examined to determine the relationship between lateral deflection and blast overpressure. The residual strength of a dished plate is examined by an extension of the concept of initial imperfections and by the recently developed extensional collapse mode analysis. The limiting effect of mixed mode crack propagation upon residual strength is then examined. This progressive analytic approach is presented in Figure 1.4.

A modest program of experimentation is conducted to determine the relationship between deflection, holing, crack propagation and residual strength. An analysis is then made of the residual strength in a modern U.S. Navy destroyer (DDG-51 Arleigh Burke Class) hit by one antiship missile amidships.





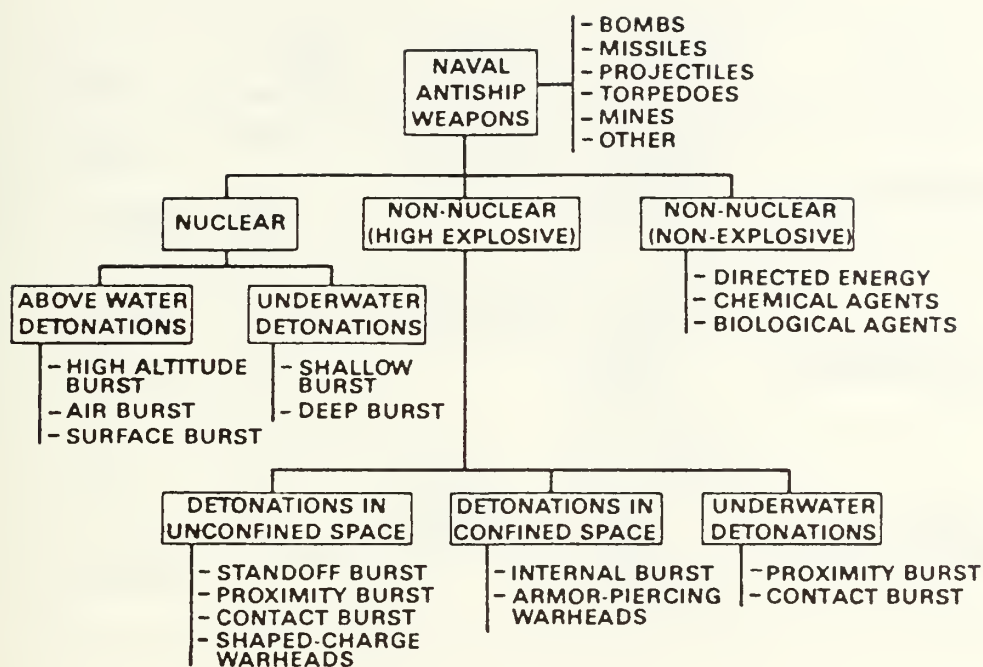


Figure 1.1: Categorization of naval antiship weapons [3]

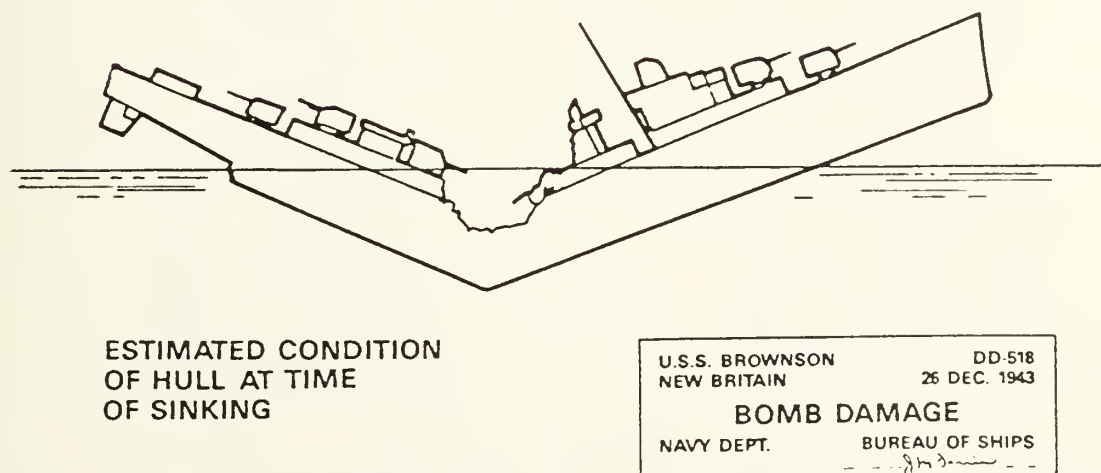


Figure 1.2: Diagram of battle damage to USS Brownson (DD-518) which sank due to loss of structural integrity [3]



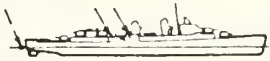
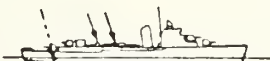

SHIP	DATE/ PLACE	DAMAGE SOURCE	MANNER OF SINKING	DAMAGE
SIMS (DD409)  2100 TONS STANDARD	5/7/42  CORAL SEA	2 BOMB HITS; 1 NEAR MISS.	JACK-KNIFED AND SANK BY STERN WITHIN 18 MINUTES.	
BROWNSON (DD518)  2100 TONS STANDARD	12/26/43  NEW BRITAIN	2 BOMB HITS; 1 NEAR MISS.	JACK-KNIFED AND SANK BODILY WITHIN 15 MINUTES.	
BUSH (DD529)  2100 TONS STANDARD	4/6/45  OKINAWA	CRASH BY 3 SUICIDE PLANES, 2 WITH BOMBS.	JACK-KNIFED AND SANK BODILY WITHIN 15 MINUTES OF FINAL HIT.	

Figure 1.3: Summary of battle damage to several World War Two U. S. destroyers which sank due to loss of structural integrity [3]

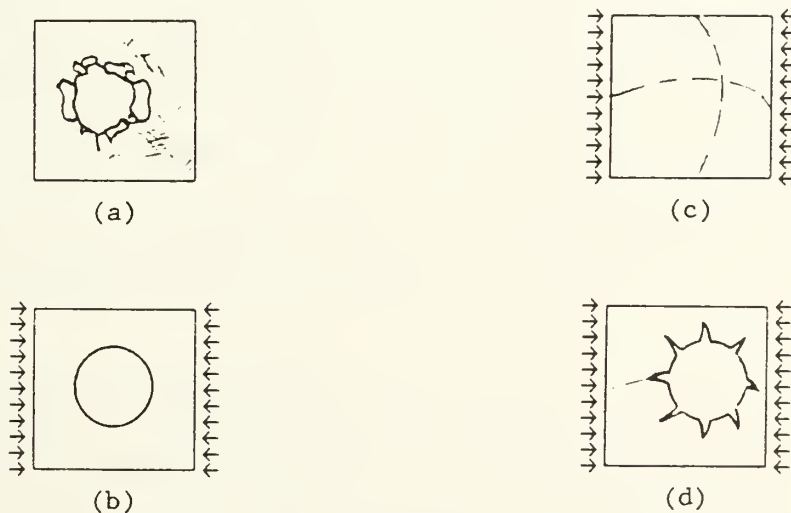


Figure 1.4: Analysis of battle damage. (a) Real damage (b) Uniaxial compressive loading of a flat plate with a central circular hole (c) Uniaxial compressive loading of a dished plate (d) Uniaxial compressive loading of a dished plate with central circular hole and initial cracks



## 2. PLASTIC LIMIT LOAD OF A FLAT PLATE

### 2.1 Introduction

Shipboard structural members such as bulkheads and decks can be modeled as thin plane sheets of homogeneous material. Such a structural member is often acted upon by forces in its plane which are much larger than the normal and shearing forces acting on its plane. If the sheet lies in the x-y plane, the non-vanishing stress and strain components are  $\sigma_{xx}$ ,  $\sigma_{yy}$ ,  $\sigma_{xy}$  and  $\epsilon_{xx}$ ,  $\epsilon_{yy}$ ,  $\epsilon_{xy}$  respectively. The loads which cause plastic collapse (yield failure) in a structure can be analytically described through the use of lower and upper bound theorems.

Structural damage consists of some combination of tearing, holing, and deflection. The compliance of a ship generally imposes a uniform displacement (which some authors describe as constant strain) boundary condition on the loaded edges. A rough upper bound limit load analysis of the effects of fully plastic fracture in a dished plate with a central circular hole is presented in Chapter 6. As an initial analysis of the effects of damage, however, a plastic limit load analysis of a flat plate with a central circular hole subjected to uniaxial compressive loading is presented here.

### 2.2 Physical Basis of Plasticity

Plastic deformation occurs when a structure experiences loads which produce stresses above the yield strength. The stress-strain curve for mild steel, shown in Figure 2.1, illustrates actual versus perfectly plastic deformation. Microscopically, plastic deformation consists primarily of shear relative to crystallographic slip-planes, with no





volume change. Three consequences of the micromechanics carry through to macromechanics: (1) incompressibility, (2) current stress is related to the increment of strain, not to the total strain as is the case with elasticity, and (3) the associated flow rule. A continuum theory of plasticity can only be applied to relatively large regions as compared with the mean free path of dislocations and the grain size (0.001 to 0.1mm), or perhaps to coherent slip bands.

There is a relation between the yield locus, which determines the state of stress at which plastic flow can occur, and the equations relating stress and strain increment for the subsequent plastic flow. The associated flow law establishes a one-to-one correspondence between the state of stress and strain rate if the yield locus is smooth with a finite curvature at each point. It has been shown to hold not only at the microscopic level but for forces and moments on structures as a whole. Once the yield strength has been reached, the current state of stress determines the ratios between the strain increments but does not define the strain. A hole in a tensile structure under plastic loading will, for non-hardening plasticity, localize the strain in a narrow band and that band will extend all the way to the nearest boundary of the part [10].

### 2.3 Limit Load Analysis

As a structure experiences general plastic deformation, its load-deflection curve becomes nearly horizontal. The limit load is the horizontal limit approached by the load-deformation curve. Although it can be very difficult to analytically determine the limit load of a structure, it is comparatively simple to determine upper and lower



bounds to the limit load.

According to the lower bound theorem, any load which is in equilibrium with a stress field such that the yield condition is not violated and the equilibrium equations are satisfied is a lower bound on the collapse load. The equations of equilibrium for plane stress are:

$$\frac{\partial \sigma_{xx}}{\partial x} + \frac{\partial \sigma_{xy}}{\partial y} = 0 \quad \frac{\partial \sigma_{xy}}{\partial x} + \frac{\partial \sigma_{yy}}{\partial y} = 0 \quad . \quad (2.1)$$

There are several ways to express the yield condition. Hodge [11] used the Tresca yield criterion which can be expressed as:

$$\max \left[ \left| \frac{\sigma_{xx} + \sigma_{yy}}{2} \right| + \sqrt{\left( \frac{\sigma_{xx} - \sigma_{yy}}{2} \right)^2 + \sigma_{xy}^2}, \right. \\ \left. 2 \sqrt{\left( \frac{\sigma_{xx} - \sigma_{yy}}{2} \right)^2 + \sigma_{xy}^2} \right] \leq \sigma_y \quad (2.2a)$$

and Gordon and McCrum [12] performed a limit load analysis using the Mises yield criterion which can be expressed as:

$$\sqrt{\frac{1}{2} \left[ \left( \sigma_{xx} - \sigma_{yy} \right)^2 + \sigma_{xx}^2 + \sigma_{yy}^2 \right] + 3\sigma_{xy}^2} \leq \sigma_y \quad (2.2b)$$

where  $\sigma_y$  is the material yield strength. In constructing lower bounds, it is frequently useful to consider discontinuous stress fields across a plane with normal  $n$  and in-plane coordinates  $s, t$ . Then the components acting across the surface  $\sigma_{nn}, \sigma_{ns}, \sigma_{nt}$  must be continuous for equilibrium, while the in-plane components  $\sigma_{tt}, \sigma_{ss}, \sigma_{st}$  need not be.

An upper bound on the limit load can be found by considering any incompressible velocity field which satisfies all velocity boundary conditions. It is frequently useful to consider discontinuous velocity fields when evaluating upper bounds, which is permissible as long as the



work associated with such a discontinuity is accounted for. The yield locus is a contour of constant value of the flow function which characterizes the yield condition. Analysis of the yield hexagon reveals that the internal energy is the product of the yield stress by the absolutely largest of the three principal strain rates. Any load which produces an external energy rate in excess of this value is an upper bound on the limit load. For the case of uniform traction (which some authors describe as constant stress), the upper bound to the limit load  $P^+$  can be expressed as:

$$P^+ = \frac{\delta W^P}{(1/A) \int \delta u^P dA} \quad (2.3a)$$

where  $A$  is the gross cross-sectional area,  $\delta W^P$  is the increment of plastic work, and  $\delta u^P$  is the increment of deflection along the line of loading. For the case of uniform displacement, the upper bound to the limit load can be simplified as:

$$P^+ = \frac{\delta W^P}{\delta u^P} . \quad (2.3b)$$

#### 2.4 Plastic Limit Load of a Holed Plate

The limit load of a flat square plate with a central circular hole, subjected to uniaxial compressive loading, can be determined within reasonable upper and lower bounds. Hodge [11] analyzed the tensile limit load of a flat square plate with a central circular hole, simply supported edges, and uniform traction boundary conditions. Figures 2.2a,b,c demonstrate that similar but orthogonal compressive or tensile loads will produce the same rigid-plastic failure. This can also be demonstrated mathematically by changing the signs of loading and



associated deflection in Eqs. 2.2 and 2.3. The rate of external work required to produce similar deflections is the same for both compressive and tensile loads.

Hodge constructed a kinematically admissible velocity field by considering a sliding of the slab out of its plane along a plane through the axis of symmetry. From the Tresca yield criterion, an upper bound  $P^+$  on the limit load of a flat plate of width  $b$  and with a central circular hole of diameter  $c$  is:

$$P^+ = P_Y \left(1 - \frac{c}{b}\right) \quad (2.4)$$

where  $P_Y$  is the tensile yield load defined as:

$$P_Y = \sigma_Y A \quad (2.5)$$

For reasonably large values of  $\frac{c}{b}$ , however, a better upper bound value must be based upon the bending model, utilizing the concept of a plastic hinge. If  $\frac{c}{b}$  is almost 1, then the holed plate could easily collapse by means of yield hinges at its four narrowest points. The yield-hinge concept can be used as a guide to obtain a reasonable velocity field. The upper bound limit load for  $\frac{1}{3} < \frac{c}{b} < 1$  thus becomes:

$$P^+ = \sqrt{2 - 4\frac{c}{b} + 3\left(\frac{c}{b}\right)^2} - \frac{c}{b} \quad (2.6)$$

A lower bound for this problem was obtained by considering the discontinuous stress field shown in Figure 2.3. The lower bound limit load for  $0 < \frac{c}{b} < 0.443$  is:

$$P^- = b \frac{(1 - c/b)(1 - \xi)}{c} \quad (2.7)$$

where  $\xi$  is a distance parameter chosen to reflect a discontinuous stress field for maximum  $P^-$ . For larger size holes, with  $0.443 < \frac{c}{b} < 1$ , the





lower bound limit load is:

$$P^- = b \frac{(1 - c/b)^2}{2c} . \quad (2.8)$$

The upper and lower bounds are combined in Figure 2.4 to describe the plate failure loading for different size holes with uniform traction. The upper and lower bounds derived by Gaydon and McCrum [12] using the Mises criterion, presented in Figure 2.5, are very similar to those derived by Hodge. Gaydon [13] also performed a biaxial limit load analysis of this case with roughly similar results.

For uniform displacement of the loaded edges, which more closely approximates shipboard structural boundary conditions, limit load analysis with Tresca criterion turns out to provide an exact solution. The upper bound displacement field is described by two 45 degree sections across the mid-plane, as shown in Figure 2.6. The lower bound is described by the constant stress regions outside the central hole, as also shown in Figure 2.6. The lower and upper bounds coincide to define the limit load:

$$P = P_Y \left[ 1 - \frac{c}{b} \right] . \quad (2.9)$$

This simple linear relationship, which corresponds to the upper bound for small holes, is depicted on Figure 2.4 along with the uniform traction upper and lower bounds. Figure 2.4 suggests that shipboard compliance, which restricts non-uniform displacement of structural plating, improves the strength characteristics of the plating.

A separate method of determining collapse load consists of simply evaluating the stress experienced by the net plate structure at the mid-plane and comparing it to the yield strength for the material. Stress concentration effects, in general, apply only to elastic behavior



and are not considered in this approach. In the case of a flat plate with a circular hole, the stress experienced in the remaining structure is increased and the uniaxial load required for yield is correspondingly decreased as:

$$P = P_y \left[ 1 - \frac{c}{b} \right] . \quad (2.10)$$

This simple "engineering" approximation is identical to the uniform displacement limit load.

The limit load theorems are based on current geometry. Structural deformations may significantly influence the boundary conditions and equations of equilibrium, producing discrepancies between the actual limit load and that based on the original shape. Ductile structural materials may not behave in a perfectly plastic manner. Thin plates, in particular, can experience considerable deformation in the elastic range which distorts the structure from the assumed plane shape prior to plastic collapse [14]. Despite these limitations, if elastic-plastic buckling has not occurred, plastic limit load analysis provides a reasonable first look at the effects of holing.



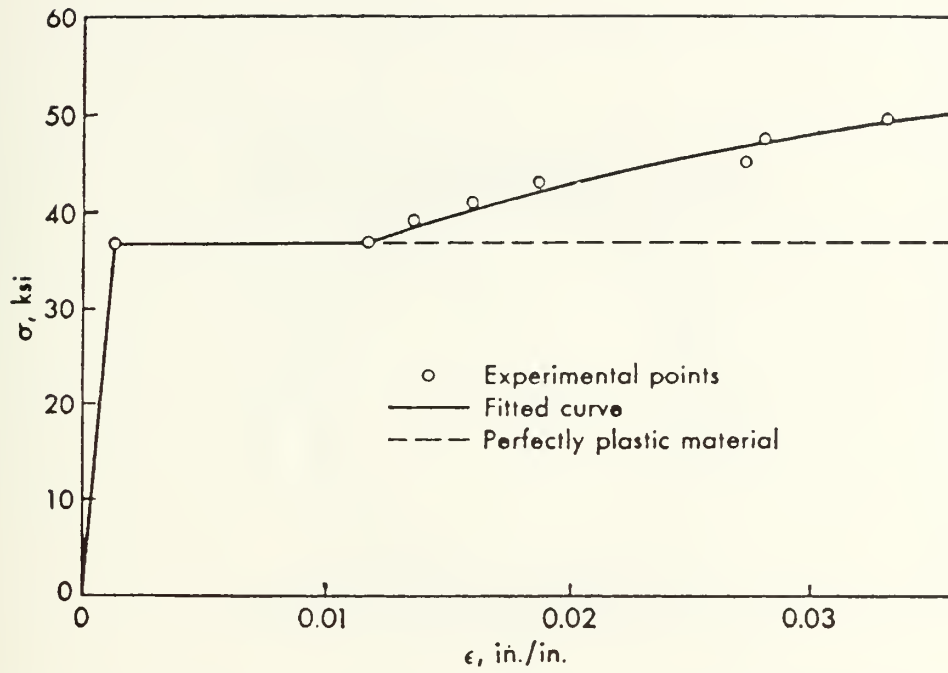


Figure 2.1: Graph of typical stress versus strain for mild steel [11]

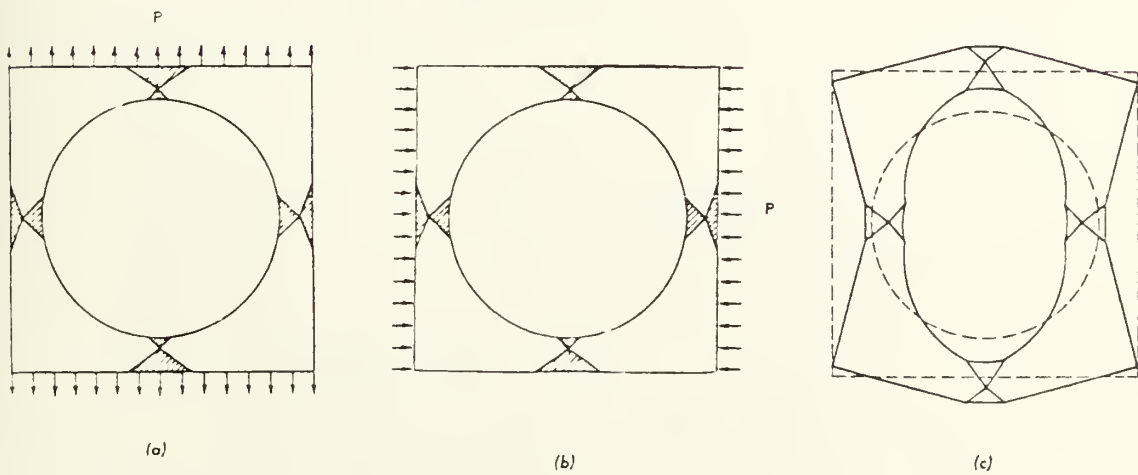


Figure 2.2: Square plate with a circular hole. (a) Tensile load (b) Compressive load (c) Uniform traction hinge type mode of collapse [11]





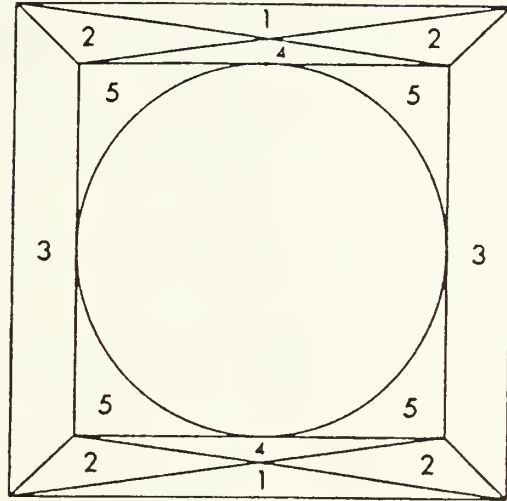


Figure 2.3: Discontinuous stress field of square plate with a central circular hole (uniform traction) [11]

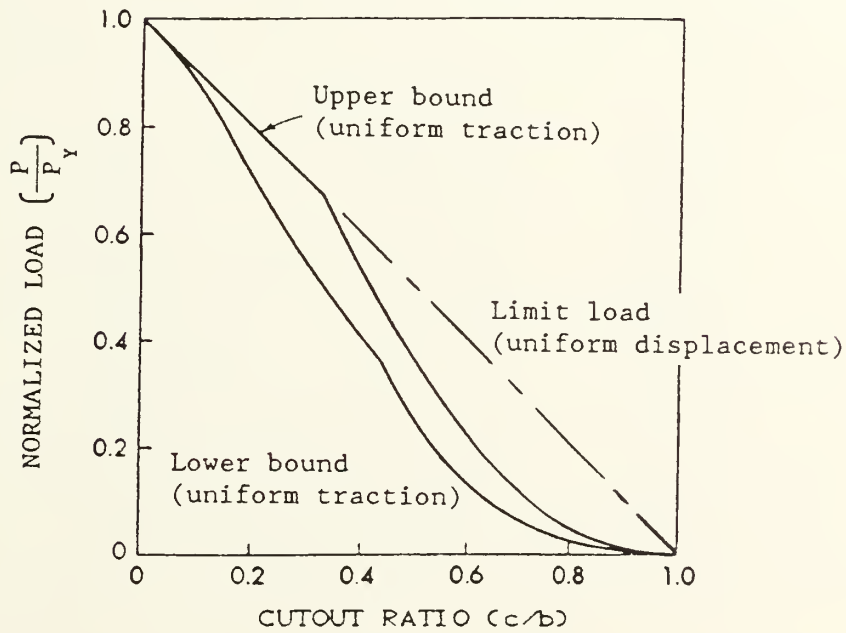


Figure 2.4: Graph of bounds for a square plate with a central circular hole using Tresca criterion [11]



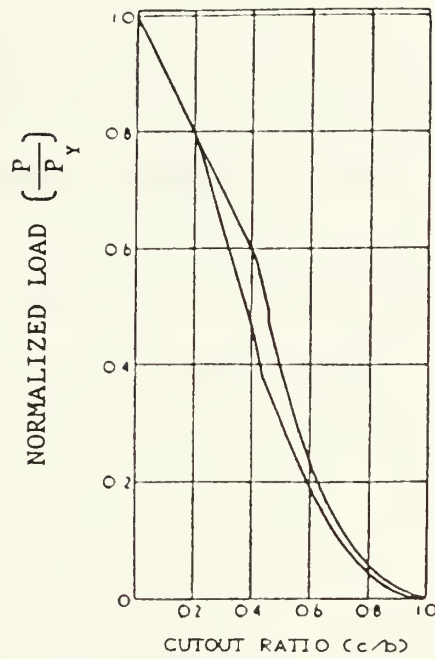


Figure 2.5: Graph of uniform traction bounds for a square plate with a central circular hole using Mises criterion [12]

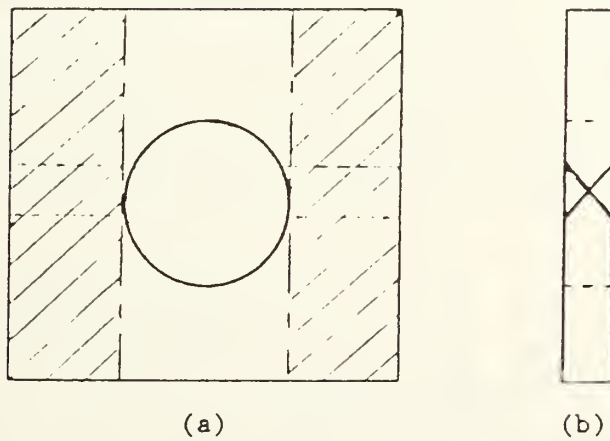


Figure 2.6: Stress (a) and displacement (b) fields for a square plate with a central circular hole (uniform displacement)



### 3. ELASTIC-PLASTIC BUCKLING AND POST-BUCKLING ANALYSIS

#### 3.1 Introduction

Elastic-plastic buckling is a typical failure pattern of thin flat plates under in-plane compressive loading. The ultimate strength of structural members defines their ability to continue providing support after suffering damage, and is reached after compressive loading has caused stresses above the yield strength. The effective width concept for unperforated flat plates describes the limiting effect of slenderness upon ultimate strength. The buckling of flat plates weakened by circular holes has been fairly extensively studied theoretically and experimentally. Kurshin and Matveev [15] made a comparative analysis of five theoretical and three experimental studies of the stability of a square plate with a central circular hole. The best agreement between theoretical analysis and experimental results was achieved by Ritchie and Rhodes [16]. Ritchie and Rhodes examined square and rectangular plates, with simply supported unloaded edges, under uniform displacement compressive loading for both buckling and post-buckling conditions. The effective width concept discussed below supports their conclusion that post-buckling strength is not significantly affected by small or medium sized holes.

#### 3.2 Effective Width Concept

For a plate subjected to uniaxial compressive loading, in general, only the parts of the plate close to the unloaded edges experience plastic yield. The stress distribution shown in Figure 3.1 is due to



the "bowing" effect in the central zone of the plate. In 1932, von Kármán postulated that the maximum load a plate with simply supported edges can sustain is reached when the edge stress equals the yield strength [17]. The effective width of the plate  $b_e$ , also shown in Figure 3.1, can be described as:

$$\frac{b_e}{b} = \frac{1}{\lambda_p} \quad \text{for } \lambda_p \geq 1 \quad (3.1)$$

where  $\lambda_p$  is the plate reference slenderness:

$$\lambda_p \cong \frac{b}{h} \frac{1.05}{\sqrt{K}} \left[ \frac{\sigma_y}{E} \right]^{1/2} \quad (3.2)$$

and where  $h$  is the plate thickness, and  $K$  is the plate buckling coefficient:

$$K = \left[ \frac{a}{mb} + \frac{mb}{a} \right]^2 \quad (3.3)$$

where  $a$  and  $b$  are the plate dimensions, and  $m$  is a wavelength parameter chosen to yield the smallest eigenvalue. A modern warship's structural plating, disregarding the effect of stiffeners, has a typical length-to-thickness ratio ( $b/h$ ) on the order of 200 to 300. With a reference slenderness ranging from 4 to 8, such plating is relatively very thin. By combining Eqs. 3.1 and 3.2, the effective width can be described as:

$$b_e = h \frac{\sqrt{K}}{1.05} \sqrt{\frac{E}{\sigma_y}} \quad (3.4)$$

With simplified dimensions of 8 feet by 8 feet, and a thickness of half an inch, warship structural plating has an effective width of roughly 1.6 feet. For plates with high slenderness values, the effective width is small and damage in the central zone has little impact on residual





strength.

### 3.3 Buckling and Post-Buckling Analysis

It is possible to analyze the initial instability of a flat plate with a central circular hole, according to Ritchie and Rhodes [16], as simply that of a flat plate. The strain energy  $U$  stored in a plate can be written as the sum of the bending and membrane strain energies:

$$U = U_b + U_m \quad (3.5)$$

where  $U_b$  is the bending strain energy and  $U_m$  is the membrane strain energy. These strain energies can be expressed in terms of the out-of-plane deflection  $w$  and the membrane stress resultants  $N_x$ ,  $N_y$  and  $N_{xy}$  as:

$$U_b = \frac{D}{2} \iint \left\{ \left( \frac{\partial^2 w}{\partial x^2} + \frac{\partial^2 w}{\partial y^2} \right) - 2(1-\nu) \left[ \frac{\partial^2 w}{\partial x^2} \frac{\partial^2 w}{\partial y^2} - \left( \frac{\partial^2 w}{\partial x \partial y} \right) \right] \right\} dx dy \quad (3.6a)$$

$$U_m = \frac{1}{2} \iint \left[ N_{xx} \epsilon_{xx} + N_{yy} \epsilon_{yy} + N_{xy} \epsilon_{xy} \right] dx dy \quad (3.6b)$$

where  $D$  is the bending rigidity of the plate,  $w$  is out-of-plane displacement, and  $\nu$  is Poisson's ratio. Ritchie and Rhodes obtained the stress resultants  $N_{xx}$ ,  $N_{yy}$  and  $N_{xy}$  in each element with respect to a unit applied displacement of the loaded edges. The magnitude of all stress resultants were then related to the loaded-edge displacement by a magnification factor, and the strains related to the stresses by Hooke's law. The deflections were represented by a single sine wave in the loaded direction, which is a reasonable approximation for plates with small holes whose behavior is similar to that of unperforated plates, but may be less accurate for plates with large holes.



Ritchie and Rhodes rewrote the strain energy in matrix form in order to solve for the buckling modes and loads. The non-trivial solutions of the simultaneous equations minimizing the strain energy were the eigenvalues of the edge displacement coefficient  $\phi$  and the corresponding eigenvectors. The solutions also satisfy the criterion for neutral equilibrium. Thus the smallest eigenvalue and its corresponding eigenvector give the buckling load or displacement and the buckling mode. Ritchie and Rhodes used a finite element analysis, with a mesh of 97 triangular constant-strain elements over one quarter of the plate, to obtain the stress distribution for both uniform edge displacement and uniform edge stress cases. The uniform displacement and uniform traction loading curves thus obtained are presented in Figure 3.2.

The post-buckling behavior was examined by a combined semi-energy and finite-element method. It was assumed that post-buckling out-of-plane deflections remain of the same form, but with varying deflection magnitude, as those obtained from the buckling solution. This assumption was considered reasonable for plates without holes if the applied load was less than about twice the buckling load. The presence of local buckles, however, causes changes in the stress system throughout the plate. These changes can be evaluated from the solution of von Kármán's compatibility equation, which relates in-plane and out-of-plane deformations in a plate by means of a stress function  $F$ , as follows:

$$\nabla^4 F = E \left\{ \left[ \frac{\partial^2 w}{\partial x \partial y} \right]^2 - \frac{\partial^2 w}{\partial x^2} \frac{\partial^2 w}{\partial y^2} \right\} \quad (3.7)$$



A second system of stresses was derived by solving von Kármán's compatibility equation, and applying the boundary conditions at the plate supported edges. A third stress system was obtained, using finite elements, by hypothetically applying a loading system around the hole edge to counteract the stresses produced by the second system. The complete membrane stress system in the plate was obtained from the superposition of these three systems:

$$n_{xx} = \phi \bar{n}_{xx1} + C_r^2 \left[ \bar{n}_{xx2} + \bar{n}_{xx3} \right] \quad (3.8a)$$

$$n_{yy} = \phi \bar{n}_{yy1} + C_r^2 \left[ \bar{n}_{yy2} + \bar{n}_{yy3} \right] \quad (3.8b)$$

$$n_{xy} = \phi \bar{n}_{xy1} + C_r^2 \left[ \bar{n}_{xy2} + \bar{n}_{xy3} \right] \quad (3.8c)$$

where the subscripts 1, 2, and 3 refer to the respective stress system.

The principle of minimum potential energy was applied by Ritchie and Rhodes to their post-buckling analysis in order to determine the buckled form. A change in natural wavelength of the rectangular plate buckled form, from two to three half-wavelengths, occurs if the hole diameter is greater than 0.35 times the plate width. Brush and Almroth [18] developed a plot of buckling coefficient  $K$  versus aspect ratio ( $a/b$ ), as shown in Figure 3.3, which presents eigenvalue curves for critical values of axial stress for simply supported unperforated plates subjected to in-plane compressive loading. A simply supported square plate would be expected to have a buckled form of one half-wavelength.

### 3.4 Ultimate Strength of A Holed Plate

A structure can continue to support loading after buckling. As



with von Kármán's analysis, the failure of a plate under a compressive edge load is assumed to occur when the maximum stress in the loaded direction reaches the yield strength. For a simple analysis, Ritchie and Rhodes defined the ultimate load as:

$$P_{ult} = \sigma_y b_e h \quad (3.9)$$

where  $b_e$  is the effective width corresponding to the yield stress  $\sigma_y$ , which is similar to Eq. (2.5). The effect of a hole in a buckled plate on the residual strength can be approximated by redistributing the compressive stresses released by the introduction of the hole over the remaining region. This produces an increase in maximum stress for a given load, and a corresponding reduction in effective width. The post-buckling stress distribution can be represented by a simple sine wave as shown in Figure 3.4 (which is similar to that shown in Figure 3.2). The increase in maximum stress due to the hole is calculated by redistributing the compressive stresses "removed" by the hole:

$$P_h = h \int_{c_t}^c \sigma_x dy \quad (3.10)$$

where  $c_t$  is the region carrying tensile stresses in the unperforated plate,  $c$  is the diameter of the hole, and  $P_h$  is the compressive load removed by the hole. The change in stress is:

$$\Delta \sigma_x = \frac{P_h}{(b - c)} \quad (3.11)$$

For a given external load  $P$ :

$$P = \sigma_{x \max} b_e h = (\sigma_x + \Delta \sigma_x) b_{ec} h \quad (3.12)$$

where  $(\sigma_x + \Delta \sigma_x)$  is the maximum stress after the introduction of the hole and  $b_{ec}$  is the corrected effective width. The corrected effective





width can then be written as:

$$b_{ec} = \frac{b_e}{\left[1 + \frac{c - ct}{b - c} + \left(1 - \frac{be}{b}\right) \left(\sin \frac{c}{2b} - \sin \frac{ct}{2b}\right) \frac{b}{b - c}\right]} \quad (3.13)$$

Figure 3.5 was produced using the relationship between applied load and effective width separately derived by Rhodes and Harvey [19]. The ultimate load for plates with various size holes was then calculated and plotted in Figure 3.6, which indicates that ultimate strength is essentially unaffected by the presence of small holes (diameter less than half the width) and is roughly equal to three times the critical buckling load  $P_{crit}$ .

No attempt was made to redistribute tension stresses released by the introduction of the hole into the analysis. This is a conservative approximation because the effect of redistributing high tensile stresses could indicate that the effective width of a plate with holing is greater than that of an unperforated plate. While it is possible that this could indeed be the case in practice, Ritchie and Rhodes suggest that it would be dangerous to advocate such a hypothesis for use in design without experimental proof.

Roberts and Azizian [9] have examined this question further and state that for uniaxial and biaxial compression the buckling load may increase with increasing size of the central circular hole due to the redistribution of membrane stresses towards the edges of the plate. The increase in buckling load is dependent upon the boundary conditions and appears significant only for plates with clamped edges. Roberts and Azizian conclude that "even though the buckling load may increase with



increasing size of the hole, it is not expected that there will be a corresponding increase in the ultimate or collapse load."

### 3.5 Comparison With Experimental Results

The experimental investigation of Ritchie and Rhodes [16] consisted of a series of tests on square and rectangular hot-dip galvanized mild steel plates to collect information on buckling loads, out-of-plane deflections, collapse loads, and strain distributions along the axes of the plates. Plate dimensions were nominally 254mm wide by 254mm or 508mm long (square and rectangular respectively) and 1.57mm thick. The unloaded vertical edges of the plate were supported in the frame by knife edges and loaded edges were supported in rollers resting on needle bearings contained in the blocks, through which the load was transmitted. The specimens were thus simply supported on all edges and subjected to uniform displacement loading. The buckling loads were estimated by obtaining the intersection of the pre- and post-buckling slopes of the load membrane strain plots. All plate specimens were loaded under uniform displacement conditions.

Ritchie and Rhodes normalized their analytic solutions and experimental results with respect to the critical buckling load. From Timoshenko and Gere [20], the critical stress of a square plate with similar boundary conditions can be described as:

$$\sigma_{crit} = \frac{2.528 h^2 E}{(1 - \nu^2) a^2} . \quad (3.14)$$

The critical buckling load can thus be normalized with respect to the tensile yield load as:



$$\frac{P_{crit}}{P_y} = \frac{\sigma_{crit}}{\sigma_y} \quad (3.15)$$

For the mild steel square plates investigated by Ritchie and Rhodes, assuming a yield strength of 30 ksi, the normalized critical buckling load is roughly 0.106.

The analysis developed by Ritchie and Rhodes describes a normalized ultimate load of roughly 0.30, with respect to the tensile yield load, for their square plates. Both the critical stress and the effective width are strongly affected by relative plate thickness. The effective width concept describes a normalized ultimate load for an unperforated square plate, of the same dimensions and material properties as tested by Ritchie and Rhodes, of roughly 0.34 with respect to the tensile yield load.

The theoretical relationship between buckling load and hole size in simply supported plates loaded by both uniform traction and uniform displacement is supported by the experimental results. The experimental results of other researchers for uniform traction buckling of a square plate are plotted in Figure 3.7 along with the analytic solution developed by Ritchie and Rhodes. The experimental results for uniform displacement buckling of a square plate are plotted in Figure 3.8, along with the analytic solutions. The change in buckling mode in rectangular plates from two to three half-waves, when the hole diameter exceeds 0.35 times the plate width, was observed in the experimental investigation. The scatter in experimental results, according to Ritchie and Rhodes, was due to the large initial imperfections in the plates. The ultimate uniform displacement loads for both square and rectangular plates are



presented in Figure 3.6 and indicate good correlation between the analytic solution and experimental results. The ultimate strength of a thin plate is essentially unaffected by the presence of small holes, and is roughly equal to three times the critical buckling load.

With regards to application, however, the experimental results indicate that the elastic-plastic ultimate strength analysis developed by Ritchie and Rhodes is slightly conservative. The observed normalized ultimate load for a thin unperforated square plate ranged from 0.34 to 0.35, which is most accurately described by applying the effective width concept. It is suggested that the Ritchie and Rhodes analysis, which accurately predicts the loss of strength associated with increased hole size, be "shifted" to coincide with the effective width solution for an unperforated plate.





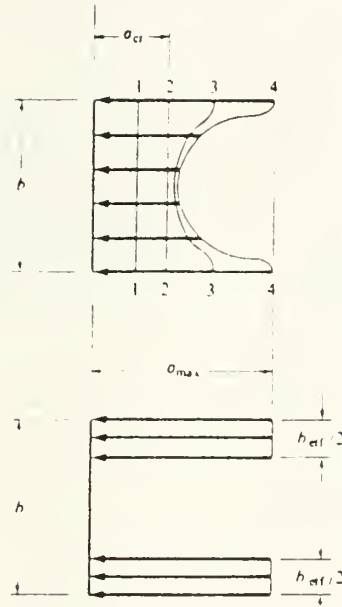


Figure 3.1: Real stress distribution and effective plate width due to in-plane compressive loading [18]

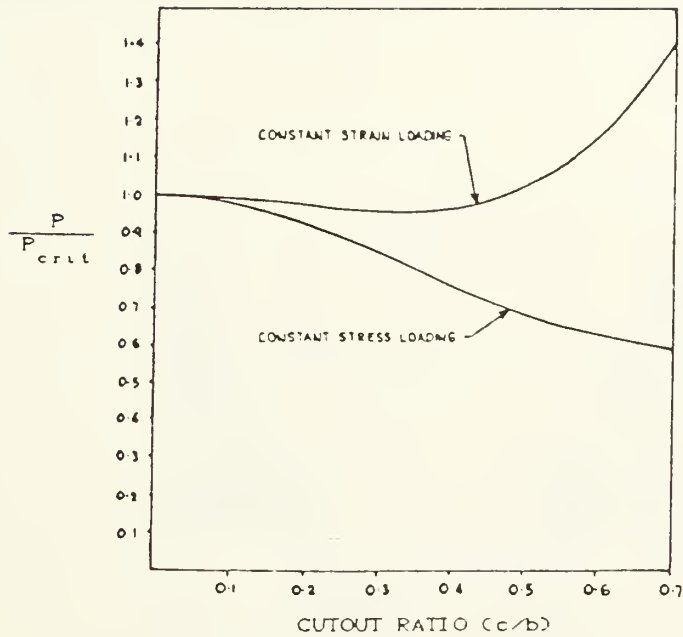


Figure 3.2: Graph of theoretical uniform traction (constant stress) and uniform displacement (strain buckling) buckling loads versus cutout ratio for square plates [16]



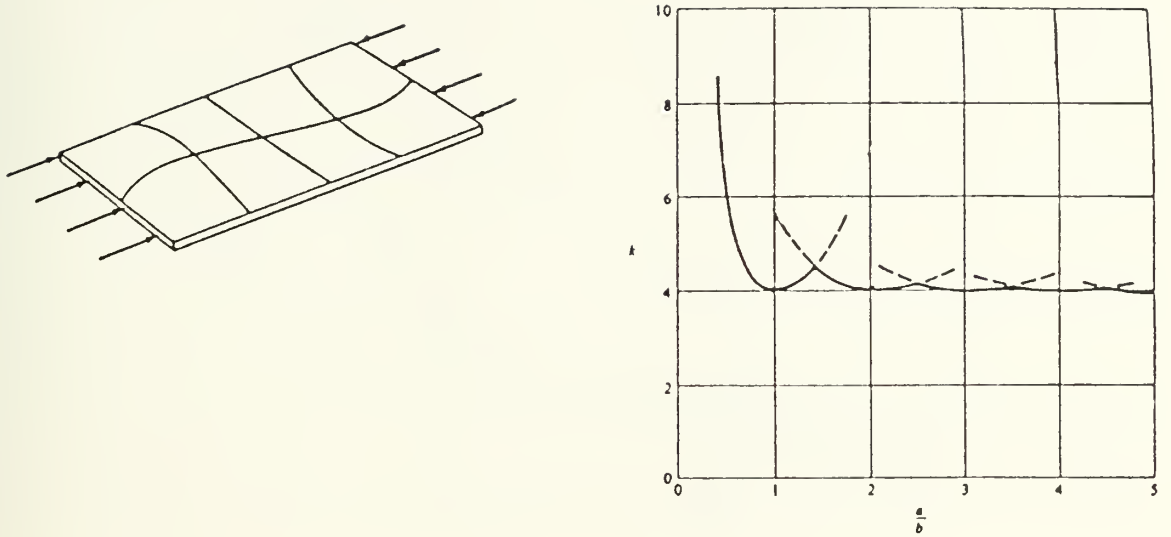


Figure 3.3: Buckled form and critical values of axial stress for simply supported plates subjected to in-plane compressive loading [18]

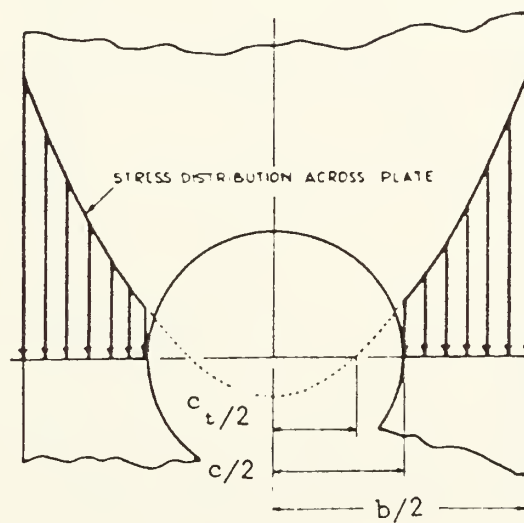


Figure 3.4: Assumed stress distribution across holed plate [16]



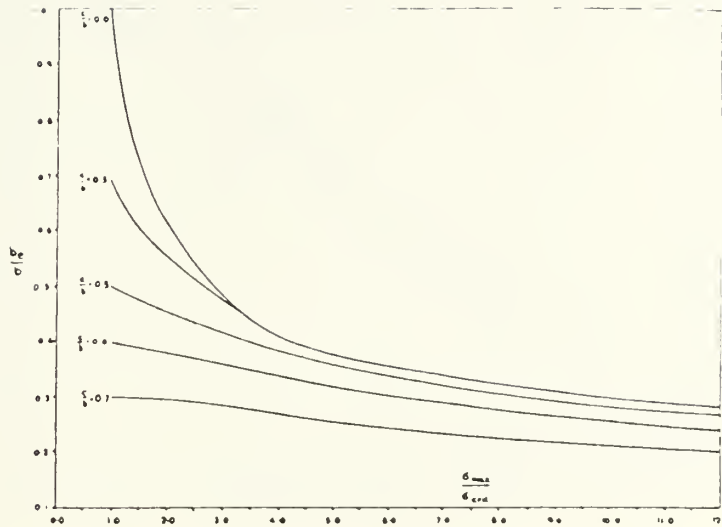


Figure 3.5: Graph of effective width versus maximum stress for various cutout ratios [16]

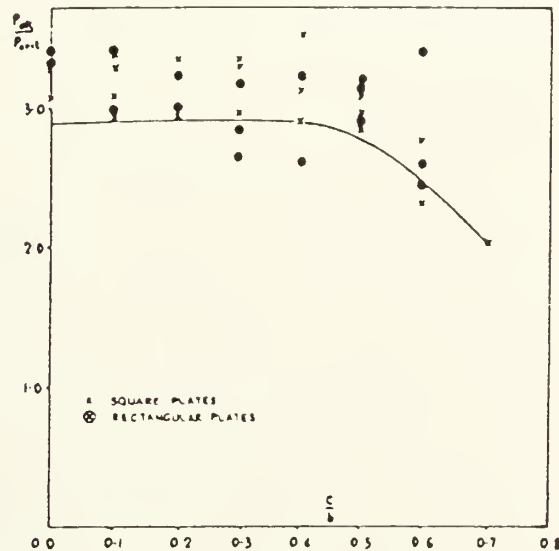


Figure 3.6: Graph of theoretical analysis and experimental results for ultimate load versus cutout ratio for square and rectangular plates [16]



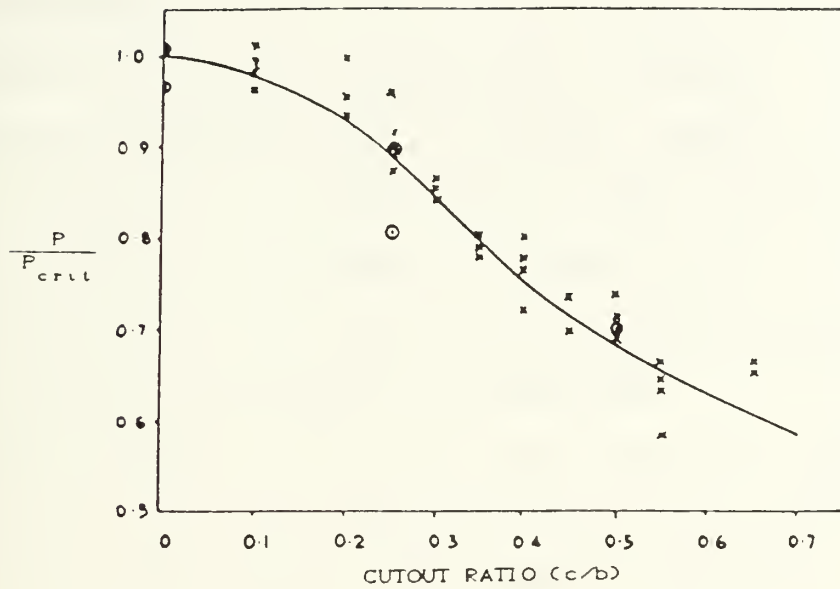


Figure 3.7: Graph of theoretical analysis and experimental results for uniform traction (constant stress) buckling load versus cutout ratio for a square plate [16]

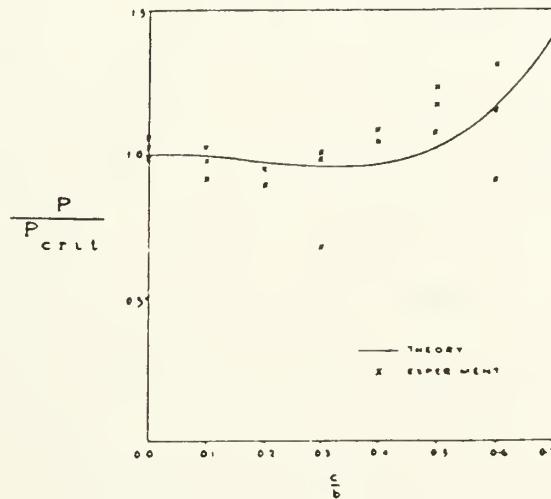


Figure 3.8: Graph of theoretical analysis and experimental results for uniform displacement (constant strain) buckling load versus cutout ratio for a square plate [16]





## 4. DISHING OF PLATES UNDER IMPULSIVE LOADING

### 4.1 Introduction

Shipboard structural members are deformed by the overpressurization associated with an internal explosion. The effects of holing produced by the initial shock wave upon residual strength of a flat plate have been investigated in Chapters 2 and 3. The quasi-static overpressurization which follows the blast produces lateral deflections in the bulkheads and deckplates of compartments.

The deformation of thin flat plates subjected to large impulsive loading has been studied extensively since World War Two. Thorough reviews of the historical development of empirical and analytical studies have been presented by several authors [21,22,23]. A number of researchers have developed good analytic techniques. In structural elements such as beams and plates, bending resistance increases along with membrane forces while the deflection is much less than the thickness of the element. As the deflection increases, however, stresses due to stretching of the middle plane dominate over bending stresses. At this stage the behavior of a beam is comparable to that of a plastic string. Perrone and Bhadra [24] developed this concept with a simple lumped mass at the midpoint. Recently, Nurick [23] developed a highly accurate membrane mode analysis based upon the lumped mass string concept. Excellent empirical relationships between deformation and impulse are developed from extensive testing conducted by Nurick and others.



#### 4.2 Dynamic Effects of an Internal Airblast

Roughly 70 percent of the energy released by a warhead detonation produces blast effects. The critical loading associated with an explosion is the high pressure discontinuity at the shock front. The shock wave produces deflection, necking, rupture and holing of plating close to the point of detonation due to the high velocity gradients across the plate surface. Rupture begins at the point of a stiffened plate structure nearest the explosion and can extend to the plates' boundaries. The shock loading is predominately normal to all structural members.

After passage and decay of the shock wave from an internal airblast, confinement of the explosion gases leads to a pressure loading which has a long duration compared to the response time of typical stiffened structures. There is no simple relation between explosive mass and pressure impulse [23]. As a result of damage to bulkheads, decks, and overheads surrounding the burst space, the gas overpressure is vented to the atmosphere and adjacent spaces and is relieved as the confinement volume increases. This "quasi-static" pressure loading is governed by the confinement volume. Figure 4.1 shows a typical trace of the pressure versus time history recorded at a point on the wall of a partially closed chamber following an internal explosion. Pressure peaks are caused by repeated reflections of the blast wave off the chamber wall. The impulse imparted by the pressure peaks is small because of their short duration, and produces negligible damage effects on internal structure and equipment [6,25].



#### 4.3 Membrane Mode Finite Element Analysis

Membrane mode approximations, in which bending is ignored, have been applied to impulsively loaded thin plates by several authors who all assumed a fixed mode shape. Nurick [23], however, has developed a model which considers lateral displacements in addition to transverse deflections, and which computes the mode shape at each time step.

The string concept forms the basis of the Nurick model. The string is sub-divided into several sections with associated lumped masses, and the acceleration is assumed to be a linear function of the velocity. As developed by Perrone and Bhadra [24], the acceleration is the second differential of displacement resulting in a first order nonlinear differential equation which is solved by numerical integration. Transverse and lateral deflections are incorporated into the equation such that the trajectory of every point on the surface remains normal to the plate surface.

The material is assumed to behave in a rigid visco-plastic manner. This can be described by the empirical relationship developed by Bodner and Symonds [26]:

$$\frac{\sigma}{\sigma_y} = 1 + \left[ \frac{\dot{\epsilon}}{D} \right]^{1/n} \quad (4.1)$$

where  $\dot{\epsilon}$  is the strain rate, D and n are material constants. Manjoine [27] investigated the influence of temperature and rate of strain on the yielding of mild steel. Bodner and Symonds applied Manjoine's work to their empirical relationship in order to define the material constants. For mild steel the material constants D and n are  $40 \text{ s}^{-1}$  and 5 respectively.

The deformed geometry of the string can be defined by a modeshape



$\phi$ , which varies with space and time. The transformed displacement is written as:

$$w_i(r,t) = \phi_i(r,t) w_c(t) \quad (4.2)$$

where  $(r,t)$  are the coordinates of space and time and  $w_c(t)$  is the central displacement. It is further assumed that the transverse velocity and acceleration fields at time  $t$  can be differentiated without taking into account the variation of the mode shape  $\phi$  with time, which is known as an instantaneous or stationary mode assumption.

The string concept is applied to plates by discretizing the plate into contours along which  $\phi$  is constant. The mode shape  $\phi$  is assumed to vary linearly with distance between contour levels. Symmetry dictates square contours for the square plates, as shown in Figure 4.2. This symmetric contour is justified by the deformation shape, shown in Figure 4.3, produced by explosive impulse loading.

It is possible to write  $(i + 1)$  dynamic equations for the lumped masses. Nurick developed an algorithm to solve the dynamic equations. The initial central velocity is computed from the initial total impulse  $I$ , which is assumed to impart a uniform velocity to the plate. The initial mode velocity is then obtained from a generalised momentum balance. The stiffness of the plate is assumed to be zero for the first time step, and the iterative solution commences with the second time step. The equations are highly non-linear, and are solved using a Newton-Raphson technique. The iterative procedure continues until a prespecified tolerance is met in order to continue to the next time step, and the forward integration is terminated when  $w_c$  equals zero. Convergence of the algorithm suggests that the final shape is reached





within  $100\mu\text{s}$ .

#### 4.4 Experimental Results and Empirical Analysis

The experimental investigation of Nurick [23] consisted of a series of tests on circular, square and rectangular plates to collect a range of deflection information on plates subjected to high impulsive loading. Plate specimens were cut from 1.6mm thick cold rolled steel and were not annealed. Plate dimensions were nominally 100mm diameter circular, 89 by 89mm square, and 113 by 70mm rectangular. Metabel was used as the sheet explosive for the experiments, and was placed on a 16mm thick polystyrene pad to attenuate the shock transmitted to the plate, provide a uniform impulse, and prevent spallation of the specimen. The specimen plate was clamped between two holding plates attached to a ballistic pendulum used to measure the impulse. A light interference method was used to measure the deflection-time history. The final mid-point deflection was measured by means of a vernier and also by a reflex metrograph.

The range of experimentation performed by Nurick was impressive. Experimentation by previous researchers did not extend beyond deflections of six to seven plate thicknesses for circular plates and eight to nine thicknesses for quadrangular plates. Nurick performed a total of 140 impulse loading experiments with deflections ranging up to twelve plate thicknesses.

The analytic prediction method developed by Nurick compares favorably with impulse loading experimental results for circular, square, and rectangular plates. The range of analytic predictions and empirical results is shown in Figure 4.4 for circular plates and Figure



4.5 for square plates. Although most of the prediction methods can do an adequate job predicting deflections with small deflection-to-thickness ratios, they display tendencies to highly over or under estimate deflections with large ratios. These over and under estimates are based upon predictions which assume a fixed mode shape.

For circular plates, the best agreement between predictions and experimental results was achieved by Nurick, Lippman [28], Perrone and Bhadra [29], and Symonds and Wierzbicki [22]. The closed-form solution for circular membranes, developed by Symonds and Wierzbicki, is a simple but accurate approximation method which disregards bending. For impulses which blanket the plate surface, their solution can be simplified as:

$$w_{cf} = \frac{.212 I}{r h [\rho \sigma_y]^{1/2}} \quad (4.3)$$

where  $w_{cf}$  is the final deflection at the center of the plate,  $r$  is the plate radius,  $h$  is the plate thickness, and  $\rho$  is the material density. For quadrangular plates, the best agreement between predictions and experimental results was achieved by Nurick, and Baker [30]. Using an energy method, Baker assumed that the energy imparted to the structure could be equated to plastic work which he then equated to the initial kinetic energy for impulsively loaded structures. Baker assumed that the force or pressure pulse was applied in a time short enough for the structure response to be only a function of the integral of the pulse, rather than the details of its time history.

It is interesting to compare and, if possible, utilize the historical data available from different impulse loading experiments. A dimensionless damage number was defined by Johnson [31]



as:

$$\alpha = \frac{\rho v^2}{\sigma_0} \quad (4.4)$$

where  $v$  the impact velocity and  $\sigma_0$  is the damage stress (mean flow stress). Table 4.1 shows the regime of damage as a function of damage number, and shows the results of some circular plate experiments. The Johnson damage number was modified by Nurick in order to non-dimensionalize dissimilar geometries. A modified damage number for circular plates can be written as:

$$\theta_c = \frac{I}{\pi r h^2 (\rho \sigma_0)^{1/2}} \quad (4.5a)$$

and a modified damage number for quadrangular plates can be written as:

$$\theta_q = \frac{I}{h^2 (a b \rho \sigma_0)^{1/2}} \quad (4.5b)$$

where  $a$  and  $b$  are breadth and length respectively of a quadrangular plate, and  $\sigma_0$  is given the value of the static yield strength  $\sigma_y$ .

Table 4.1: Typical Johnson's Number Damage Regime  
(mild steel at room temperature impacted by a projectile) [31]

ft/sec	$\alpha$	regime
2.5	$10^{-5}$	{ quasi-static elastic
25	$10^{-3}$	plastic behaviour
250	$10^{-1}$	slow bullet speeds
2 500	$10^1$	extensive plastic deformation
25 000	$10^3$	hypervelocity impact

For plates of equal area and thickness subjected to equal total impulses, the midpoint deflection of the circular plate exceeds



that of the square plate, which in turn exceeds that of the rectangular plate. A dimensionless plot of deflection-to-thickness ratio versus modified damage number  $\theta_q$  for quadrangular plates is presented in Figure 4.6. A least squares correlation analysis of the experimental results indicates that Nurick's experimental results are consistent with previous data, and that a relationship exists between the impulse a given plate is exposed to and the deformation it experiences.

Based upon the extensive range of consistent experimental results, it is possible to develop an empirical solution to the deflection problem. A least squares analysis of the circular plate experimental data yields:

$$\left[ \frac{w_{cf}}{h} \right]_c = 0.425 \theta_c + 0.277 \quad (4.6a)$$

where the number of data points was 109 with a correlation coefficient of 0.974. A least squares analysis of the quadrangular plate experimental data yields:

$$\left[ \frac{w_{cf}}{h} \right]_q = 0.236 \theta_q + 0.001 \quad (4.6b)$$

where the number of data points was 156 with a correlation coefficient of 0.984. The empirical relationships can be simplified to:

$$\left[ \frac{w_{cf}}{h} \right]_c = 0.425 \theta_c \quad (4.7a)$$

$$\left[ \frac{w_{cf}}{h} \right]_q = 0.236 \theta_q \quad (4.7b)$$

as a useful "engineering" approximation.

The excellent correlation of the empirical formulas indicate that they can be readily applied to engineering analyses. The linear nature of the closed-form deformation solution developed by Symonds and





Wierzbicki, and others, supports the use of a linear empirical relationship based upon a modified Johnson's damage number. Extensive deformations can produce tearing along the edges of the plate or hoīng in the center of the plate. The maximum non-tearing deflection-to-thickness ratios during Nurick's testing were 11.60 and 11.97 for circular and quadrangular plates respectively. This tearing along the clamped boundaries indicates that both analytical and empirical prediction methods are limited to modified damage values of  $\theta_c \leq 25$  for circular plates and  $\theta_q \leq 50$  for quadrangular plates.



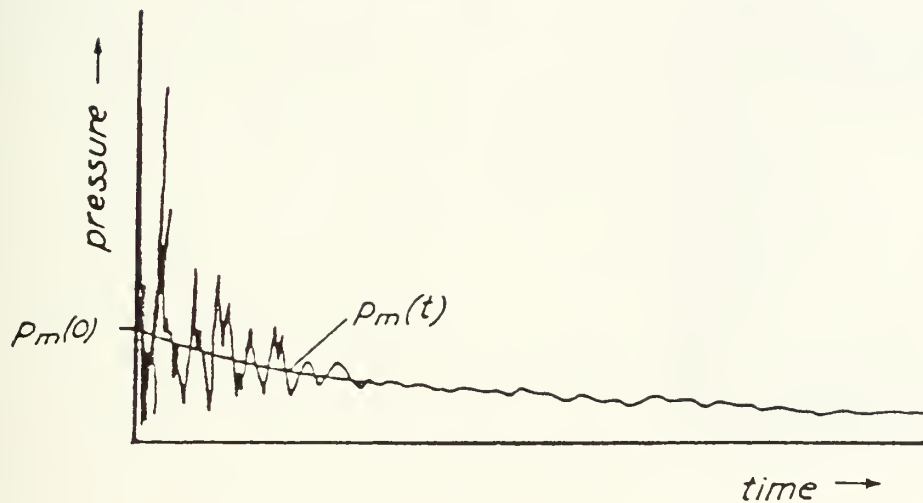


Figure 4.1: Graph of pressure versus time response recorded at a point on the wall of a partially closed chamber following an internal explosion [25]

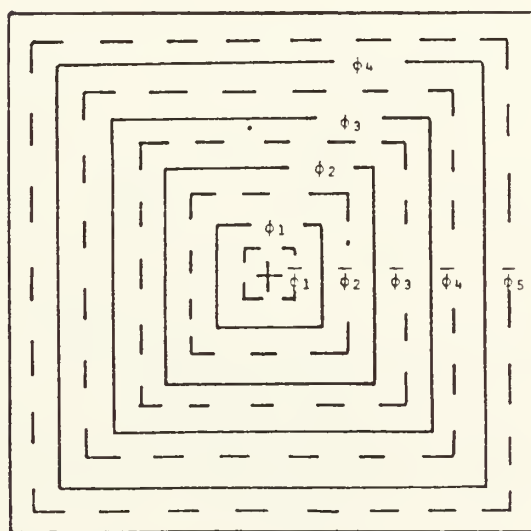


Figure 4.2 Analytic model showing discretization of a square plate [23]



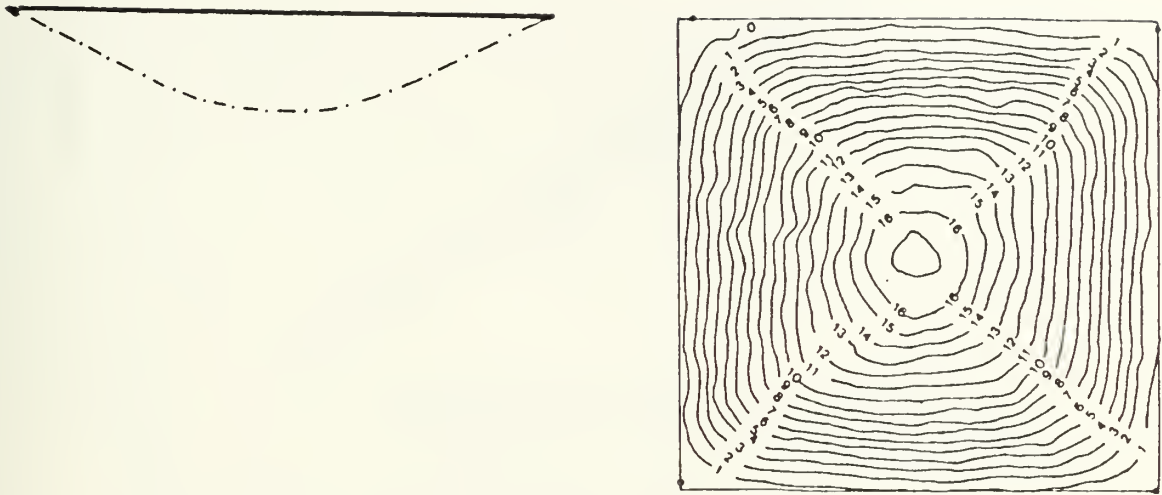


Figure 4.3 Final mode profile and contour plot of a typical explosive test for a square plate [23]

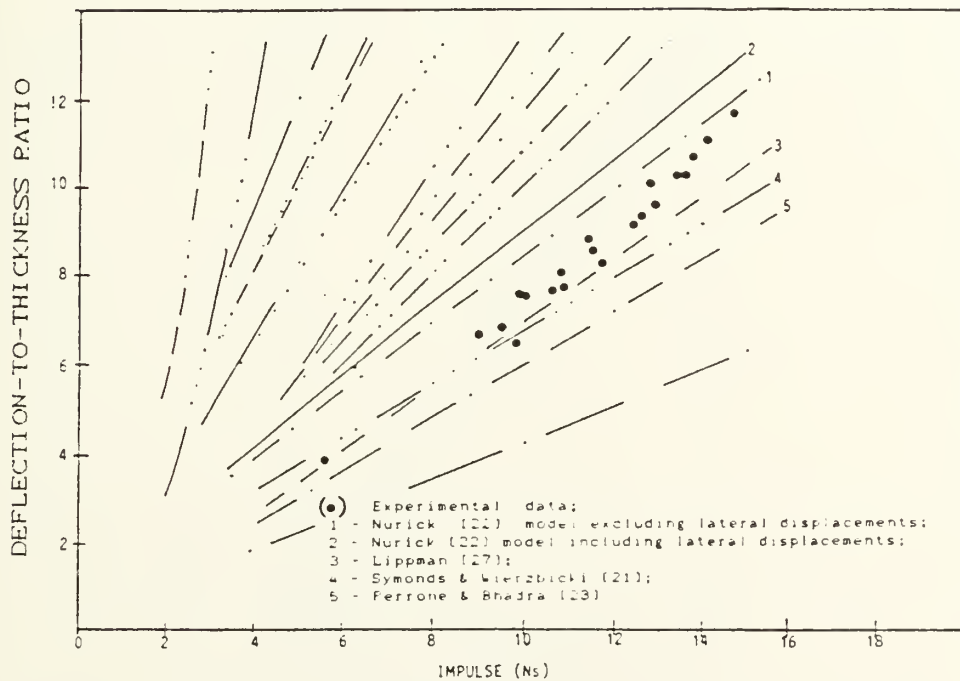


Figure 4.4: Graph of analytic solutions and experimental results for deflection-to-thickness ratio versus impulse for circular plates [23]



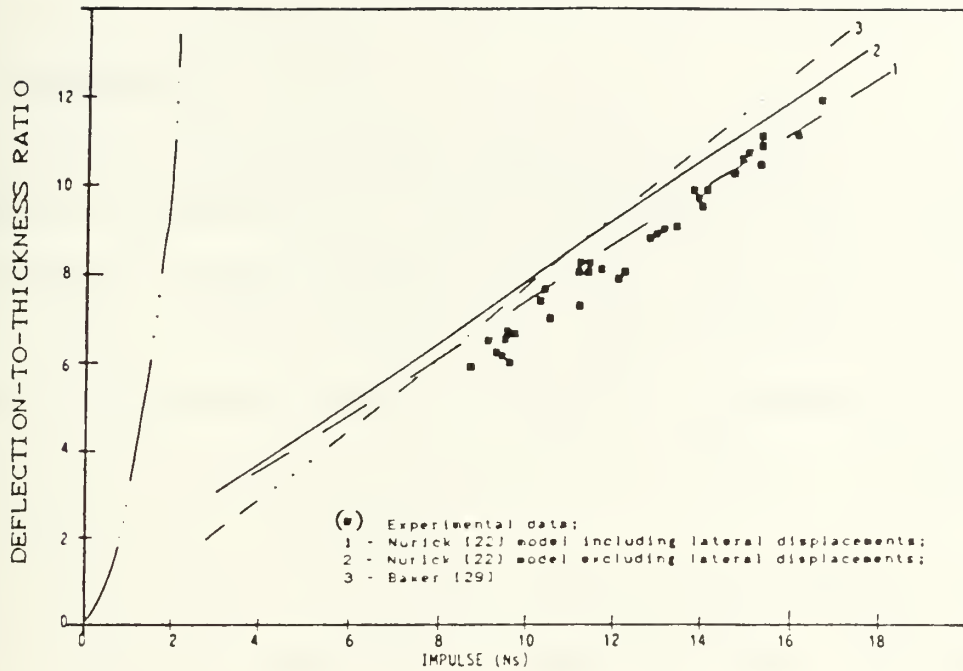


Figure 4.5: Graph of analytic solutions and experimental results for deflection-to-thickness ratio versus impulse for square plates [23]

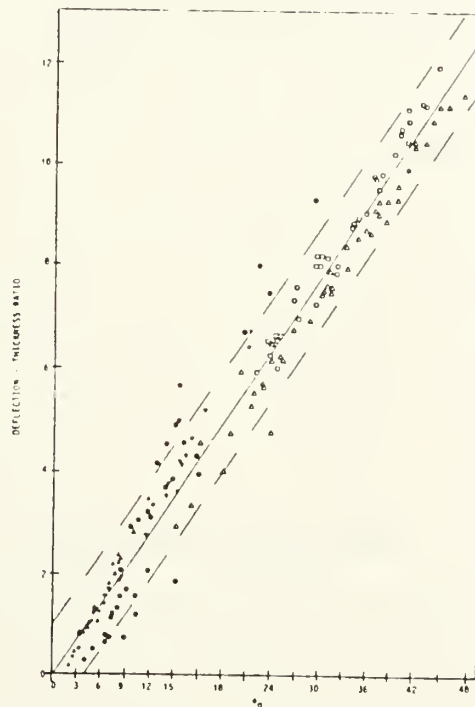


Figure 4.6: Graph of deflection-to-thickness ratio versus dimensionless damage number  $\theta_q$  for quadrangular plates [23]





## 5. STRENGTH OF A DISHED PLATE

### 5.1 Introduction

Despite the large lateral deformations suffered by shipboard bulkheads and deckplates as a result of impulsive loading, the plating can continue to support normal service loads. The dishing of thin flat plates into a shell was related to such parameters as material properties and explosive impulse in Chapter 4. By examining large scale elastic-plastic deformation mechanisms it is possible to describe the buckling behavior of a thin shell.

An out-of-flatness plate with a small initial deflection does not react to in-plane loading like an ideal flat plate. The effect of initial out-of-plane deformations is generally to reduce the peak load of the plate and bias the mode of failure towards the initial shell shape. The effect of initial imperfections upon the ultimate strength of plates offers some insight into the effect of large scale dishing. The residual strength of a thin shell with large initial deformation (on the order of 5 to 15 plate thicknesses) is first analyzed as a simple extension of the concept of initial imperfections. An extensional collapse mode analysis is then developed as a simple closed-form solution which accounts for actual deformation mechanisms.

### 5.2 Physical Basis of Deformation Mechanisms

The yield load of a plate and the elastic-plastic buckling load provide two limits to plate strength. The onset of plasticity is affected by both the in-plane and plate bending stress components.



Plasticity becomes more significant as the initial out-of-plane imperfections become larger causing surface and membrane yield to occur earlier. The interaction of membrane and bending stresses, with initial imperfections, produces an early loss of stiffness and reduction in peak load below the ideally planar elastic buckling load [17].

Although the ultimate strength of a plate with very slight initial imperfections remains reasonably close to that of an ideal flat plate, the effects of larger imperfections (on the order of the plate thickness) can be significant [17]. Von Kármán developed the effective width concept (presented in Chapter 3) to describe the stress distribution produced in a simply supported plate subjected to uniaxial compressive loading. The influence of geometrical imperfections has been incorporated into a von Kármán analysis by several authors, as shown in Table 5.1. Initial deflections of the plate lead to a marked reduction of the peak load, especially for thin plates with reference slenderness  $\lambda_p$  less than 1.5. From Eq. 3.2, the reference slenderness is:

$$\lambda_p \cong \frac{b}{h} \frac{1.05}{\sqrt{K}} \left[ \frac{\sigma_y}{E} \right] . \quad (5.1)$$

Rectangular plates restrict the failure mode and generally have greater stiffness than square plates, but suffer a steeper post-buckling behavior [17].

In order to understand the true collapse behavior of a shell subjected to uniaxial compressive loading, the effect of out-of-plane deformations on the in-plane stress state of the plate must be considered. In the large deflection regime, in general, in-plane and



out-of-plane displacements and hence stresses and strains interact. As a result of dishing, the length of the plate center line becomes greater than the boundary length and membrane tensions develop in both plate directions. Membrane action becomes more and more dominant as out-of-plane deflections become larger [17].

Table 5.1: Empirical relationships to describe the effect of small initial imperfections upon effective plate width [17]

Winter,	$\frac{b_e}{b} = \frac{1}{\lambda_p} \left[ 1 - \frac{0.22}{\lambda_p} \right]$	for $\lambda_p \geq 0.67$
Faulkner,	$\frac{b_e}{b} = \frac{1.05}{\lambda_p} \left[ 1 - \frac{0.26}{\lambda_p} \right]$	for $\lambda_p \geq 0.55$
Gerard,	$\frac{b_e}{b} = \frac{0.82}{\lambda_p^{0.85}}$	

### 5.3 Large Initial Imperfection Analysis

Extensive research has been conducted in the last twenty-five years on the ultimate load behavior of box girder structures [32,33,34]. This research has followed a series of structural failures involving merchant ships (large ore carriers in rough seas near Japan) [33] and large box girder bridges in Europe [34]. Frieze, Dowling and Hobbs [32] have developed a large deflection elastic-plastic analysis to examine the behavior of plates in compression.

The analytic method developed by Frieze et al. uses a modified von Kármán analysis to account for material non-linearity and the effects of residual stresses and initial out-of-plane deflections. The governing equations were solved by computer processing using an iterative finite



difference procedure. Frieze et al. performed a parametric study examining the collapse behavior of a uniaxially loaded plate. This analysis indicates that the influence of aspect ratio ( $a/b$ ) is dependent upon both the magnitude of the initial deformation and the slenderness ratio. Although the in-plane restraint along unloaded edges (constrained or unrestrained) has little effect on the behavior of stocky plates, the analysis indicates that slender plates with constrained edges retain their strength better than with unrestrained edges. Figure 5.1 shows that this is especially true for plates with large initial deformations. Slender plates, in particular, suffer from the weakening effects of initial deformations which generally dominate the effects of residual stresses.

The residual strength of a thin shell can be extrapolated from theoretical and empirical analyses which have been performed for modest initial deformations. It is not possible to directly apply the analyses because shipboard structural plating is very thin. The analyses can be extrapolated by applying the von Kármán effective width concept to describe the loss of strength for unperforated flat plates with increasing slenderness. The theoretical analysis of Frieze et al. is summarized by Figure 5.2, which presents six different curves of ultimate load versus slenderness  $\beta$  for different levels of initial dishing. The slenderness value  $\beta$  is defined as:

$$\beta = \frac{b}{h} \sqrt{\frac{\sigma_Y}{E}} \quad (5.2)$$

which is roughly twice the plate reference slenderness  $\lambda_p$  for a square plate. The slenderness ratio  $\beta$  for shipboard structural plating,





disregarding the effect of stiffeners, ranges roughly from 9 to 15. Ueda et al. [35] also examined the effects of initial deformations and residual stresses on the compressive strength of square plates, and conducted a modest program of experimentation. Large-deflection, elastic-plastic analyses were performed using an incremental finite element technique. Ueda's theoretical and experimental research supports Freize's analysis, as shown in Figure 5.3, and by extrapolation suggests that the normalized ultimate load would decrease for a thin shell with large initial deflections by roughly 10 percent from that of a flat plate with similar slenderness. The plate critical buckling curve is included in both Figures 5.2 and 5.3 for comparison purposes. Even with large initial imperfections, the ultimate strength of slender plates is greater than the critical buckling load.

#### 5.4 Extensional Collapse Mode Analysis

A structure can absorb crushing work through local plastic folding with bending and extensional deformation. Minorsky [36] examined the ship collision problem, with an analysis of empirical data from several dozen reported casualties, and found that plastic work dissipation is linearly related to the volume of damaged members. Although useful for studying major collisions, Minorsky's method is not valid for structural failure of a local nature. The theory of extensional collapse of plate elements was developed by Hayduk and Wierzbicki [37] and others in the early 1980's to examine the crush behavior of individual members during crushing. Extensional collapse mode analysis is described here in order to determine the average load-carrying capability in structural plating



crushed beyond the ultimate load.

Ships are generally constructed of plate-like structures, as shown in Figure 5.4. During deformation, the edges of the structure can be considered hinge lines, as can the horizontal limits of the buckling region. Crushing work is dissipated through plastic bending of adjacent plates about the horizontal hinge lines connecting them and through shape distortion of each plate. The energy-balance postulated by Wierzbicki and Abramowicz [38] indicates that zones of bending and extensional deformation, which are restricted to a small fraction of the total area of the structure, dissipate essentially all of the work done by the applied load during the crushing deformation mode.

In the propagating hinge line deformation mode (Mode I), extension is limited to the neighborhood of the hinge line. Displacement fields must be described by a continuous and smooth function across a propagating hinge line. The quasi-inextensional collapse mode of a L-shaped angle element is shown in Figure 5.5. Wierzbicki and Abramowicz described the individual dissipation energies associated with the deformation of a toroidal shell, horizontal hinge line, and inclined hinge line through complete folding of the section. In the basic folding mechanism of a L-shaped angle element there are eight horizontal hinge lines, two inclined hinge lines, and one toroidal shell section. The resulting theoretical crushing strength of a L-shaped element is thus given by:

$$\frac{P_m}{M_o} = 12.04 \sqrt[3]{\left[ \frac{b}{2h} \right]} \quad (5.3)$$

where  $P_m$  is the mean crushing load and  $M_o$  is the fully plastic yield



moment defined as:

$$M_o = \sigma_o \frac{h^2}{4} \quad (5.4)$$

where the flow stress  $\sigma_o$  can be reasonably approximated as:

$$\sigma_o = 0.9 \sigma_{UTS} . \quad (5.5)$$

Short-angle columns commonly fold up and fail in an asymmetric mode unless very large imperfections are introduced in the shape of the symmetric modes [37].

In the stationary hinge line deformation mode (Mode II) the edges of the structure remain stationary while the side plates undergo rigid-plastic distortion. Plate distortions consist of either extensive in-plane compression or in-plane extension. Hayduk and Wierzbicki assumed that there is a linear variation of the velocity field in the horizontal y-direction, as shown in Figure 5.6, and developed the individual dissipation energies associated with the deformation of a plate, stationary horizontal hinge and stationary inclined hinge through complete folding of the section.

Hayduk and Wierzbicki applied the extensional collapse mode analysis to a x-shaped cruciform structural element. A cruciform is constructed of four flanges which are rigidly joined along the initially vertical edge. A cruciform element reasonably simulates the boundary conditions on a plate in a typical shipboard compartment. Within the folding zone, the joint line becomes an inclined hinge fixed in the material. In Mode II crushing of a cruciform there are eight trapezoidal distortion sections, sixteen stationary horizontal hinge lines, and four stationary inclined hinge lines. An upper bound to the



crushing strength of a cruciform element can thus be described as:

$$\frac{P_m}{M_o} = 20.05 \sqrt{\left[ \frac{b}{2h} \right]} . \quad (5.6)$$

This least upper bound is based upon a minimum energy analysis which indicates that folding will occur with a zone of half-wavelength H:

$$H = \sqrt{\left[ \frac{\pi b h}{4} \right]} . \quad (5.7)$$

The upper bound analysis also indicates that the energy dissipated at the inclined hinge lines is negligible for a sufficiently large length-to-thickness ratio.

A lower bound on the crushing strength of a cruciform can be similarly derived by noting that a continuous joint along the vertical edge of a cruciform increases the column strength as compared to a column composed of two unjoined L-shaped elements. From the Mode I analysis of a single L-shaped element, a lower bound to the crushing strength of a cruciform can be described as:

$$\frac{P_m}{M_o} = 24.08 \sqrt[3]{\left[ \frac{b}{2h} \right]} . \quad (5.8)$$

Careful inspections of several crushed cruciforms, such as the one shown in Figure 5.7, reveal that the actual collapse mechanism is a combination of the two basic deformation modes. Hayduk and Wierzbicki developed a modified Mode II model, and described the mixed-mode crushing strength of a cruciform as:

$$\frac{P_m}{M_o} = 22.96 \sqrt[3]{\left[ \frac{b}{2h} \right]} + 2.88 \sqrt[3]{\left[ \frac{b}{2h} \right]^2} . \quad (5.9)$$

The Hayduk and Wierzbicki extensional collapse mode solutions for





cruciform failure are based upon complete folding of the structure.

This extensional collapse mode analysis of a cruciform can be applied to the residual strength of a dished plate. The typical load-deflection characteristics of a crushed cruciform, shown in Figure 5.8, indicate that the ultimate strength of a cruciform with initially flat side plates is rapidly reached during uniaxial loading. The post-buckling and folding behavior after the ultimate strength is reached "reinforces" the cruciform and allows it to continue to support loading during repeated folding. Since the collapse mode analysis indicates that folding will occur along a zone of width  $2H$  defined by Eq. 5.5, dishing may not significantly reduce a plate's ultimate strength because the dished shape does not encourage the folding. Although dishing may reduce a plate's ultimate strength, it is postulated that the mean crushing load  $P_m$  which the structure can support is little affected by the dishing.

The extensional collapse mode analysis equations can be rewritten to provide normalized loads for shell crushing. The mean crushing load is normalized with respect to the tensile yield load. By assuming that the strength of a single dished plate can be considered equal to one-half that of a cruciform, the upper bound can be expressed as:

$$\frac{P_m}{P_Y} = \frac{\sigma_o}{\sigma_Y} \frac{2.51 h (b/2h)^{1/2}}{b} \quad (5.10a)$$

the lower bound can be expressed as:

$$\frac{P_m}{P_Y} = \frac{\sigma_o}{\sigma_Y} \frac{3.01 h (b/2h)^{1/3}}{b} \quad (5.10b)$$

and the mixed-mode solution can be expressed as:



$$\frac{P_m}{P_Y} = \frac{\sigma_o}{\sigma_Y} \frac{2.87 h (b/2h)^{1/3} + 0.36 h (b/2h)^{2/3}}{b} \quad (5.10c)$$

A modern warship's structural plating, disregarding the effect of stiffeners, has a typical length-to-thickness ratio ( $b/h$ ) on the order of 200 to 300. From the upper and lower bound analysis for a warship's structural plating, the normalized mean crushing load ranges from 0.05 to 0.13.

The extensional collapse mode analysis can be applied to a holed shell. Since the width of the local folding zone is much smaller than the height of the typical cruciform, as shown in Figure 5.9, the "wing areas" can be considered ineffective in terms of both extensional and bending energy. By assuming that the fold is made through the hole region, the effective plate half-width can be reduced by the radius of holing. For Eqs. 5.10a - 5.10c only the half-width-to-thickness ratio ( $b/2h$ ) in the numerator is reduced by holing. The extensional collapse mode analysis can then be applied using the reduced half-widths.

### 5.5 Comparison With Experimental Results

The experimental investigation of Hayduk and Wierzbicki [37] consisted of a series of tests on thin copper cruciform specimens. Specimens were constructed of two L-angle elements of 0.014 inch thick copper sheeting butted along the bend line and soldered with common 60-40 lead-tin solder. Specimen length varied from 2.0 to 4.0 in. while plate half-widths varied from 1.0 to 2.0 in., for a length-to-thickness ratio which varied from 143 to 286. The unloaded vertical edges of the cruciform were clamped at the top and bottom to prevent specimen



twisting during loading. During quasi-static loading the specimens were routinely crushed from 40 to 60 percent of their original length.

The extensional crushing mode analysis is supported by the experimental results. Figure 5.10 presents the experimental data and the upper, lower and mixed-mode solutions for crushing of copper cruciforms and other elements. The experimental data for cruciforms are shown by open circles. The scatter of experimental data indicates that the cruciforms failed according to a varying combination of collapse mechanisms. The collapse mechanisms are sensitive to imperfections. Indications of fracture at the joint in some test pieces explains some of the scatter below the mixed-mode solution. Despite the scatter of data, all experimental results for cruciforms lie within the upper and lower bound solutions to normalized mean crushing load. Amdahl [39] performed a similar series of tests on larger steel cruciforms which also support the validity and usefulness of extensional crushing mode analysis.



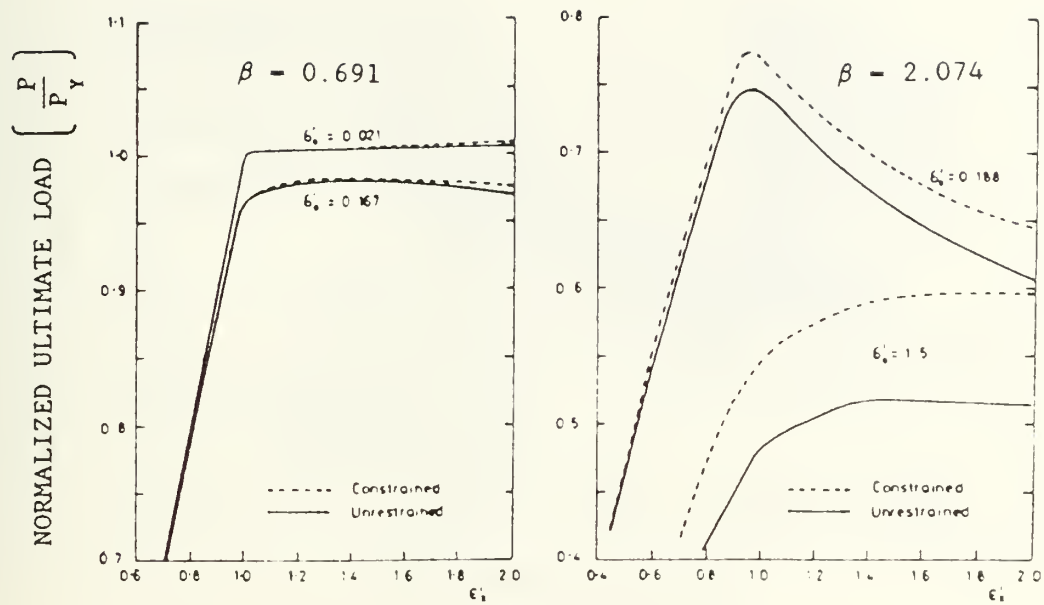


Figure 5.1: Graphs of theoretical ultimate load versus strain for square plates with different slenderness values [32]

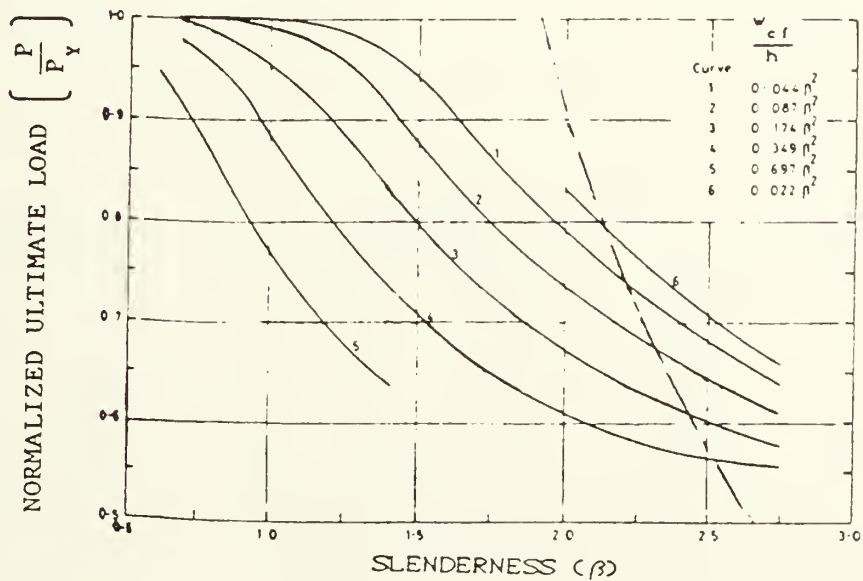


Figure 5.2: Graph of theoretical ultimate load versus slenderness for square constrained plates with different initial deflections [32]





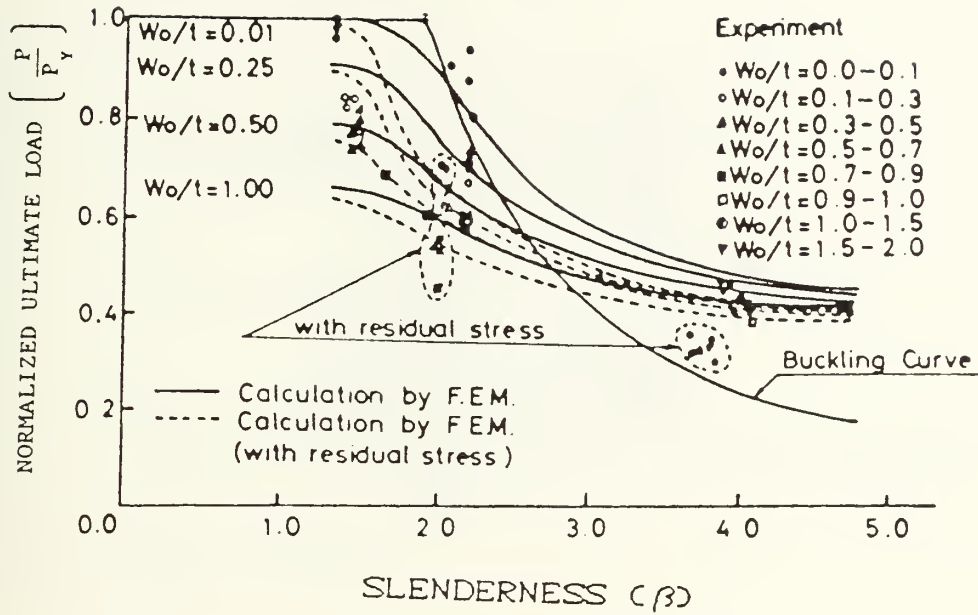


Figure 5.3: Graph of theoretical analysis and experimental results for ultimate load versus slenderness for square plates including the effects of initial deflections and welding residual stresses [33]

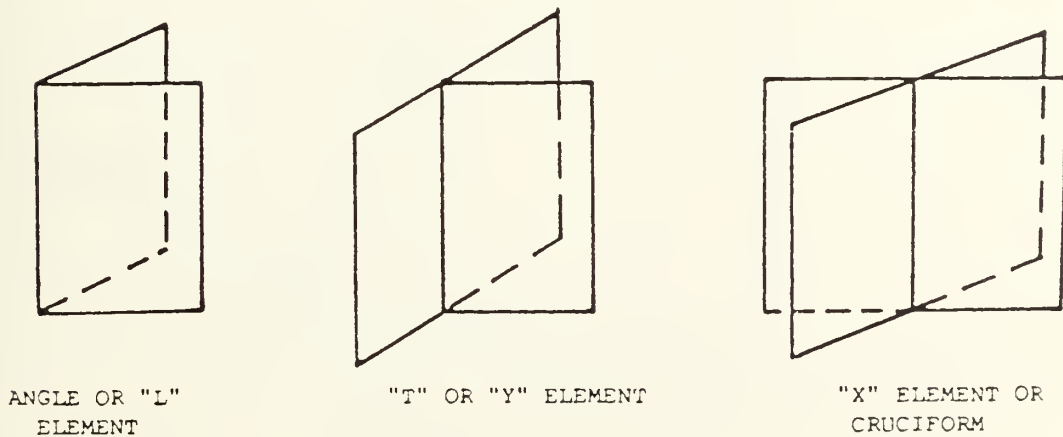


Figure 5.4: Typical structural elements



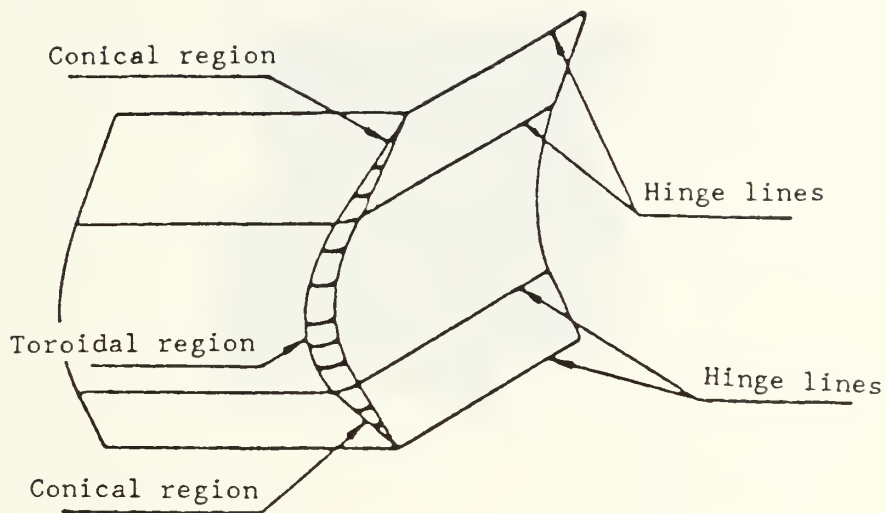


Figure 5.5: Basic folding mode of a L-shaped angle element with a continuous and smooth displacement field [37]

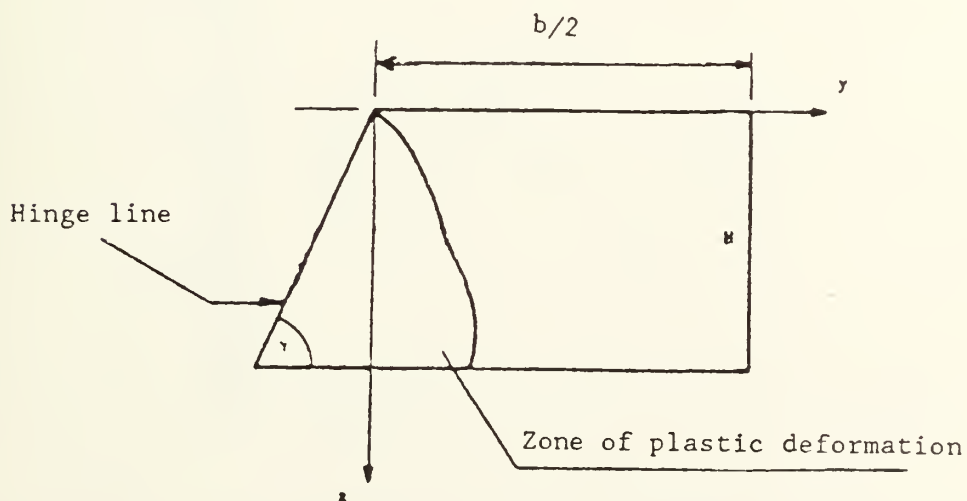


Figure 5.6: Plastic distortion of a rectangle into a trapezoid [37]





Figure 5.7: Photograph of partially crushed cruciform

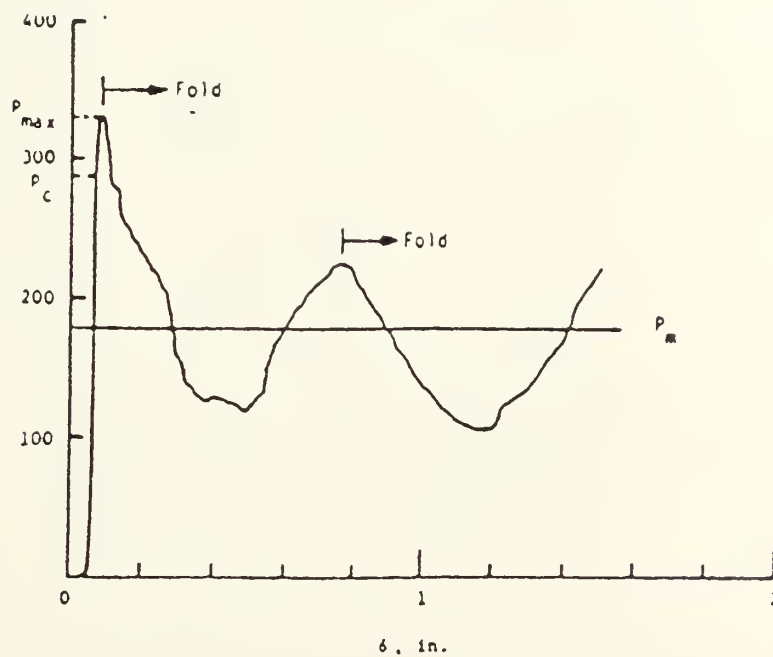


Figure 5.8: Graph of typical load versus deflection characteristics of a crushed cruciform [37]



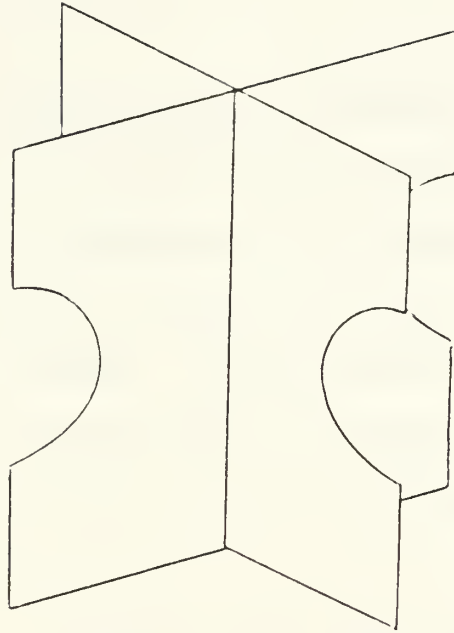


Figure 5.9: Cruciform with holed half-plates

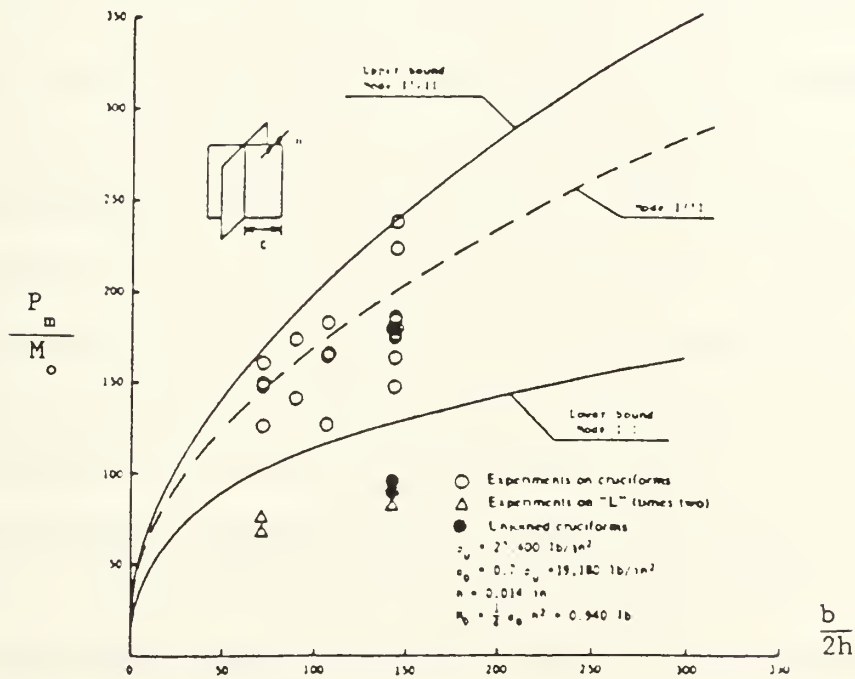


Figure 5.10: Graph of theoretical analysis and experimental results for mean crushing strength versus half-plate length-to-thickness ratio for cruciforms [37]





## 6. MIXED MODE CRACK PROPAGATION

### 6.1 Introduction

The hole edge produced during the fracture and tearing of metal plates associated with an internal airblast is not smooth. Although the hole can reasonably be considered to be circular for some forms of analysis, it is important to examine the effect of a ragged and torn edge upon residual strength. Initial cracks of various sizes will emanate from around the rough edge of the hole. Crack growth under loading (monotonic or cyclic) may limit the residual strength of the structure.

The initiation of cracks during holing and overpressurization associated with the airblast is a complex dynamic situation. The deformed plate can be considered a thin shell. Crack initiation and propagation from the torn edges associated with holing and fragmentation occurs in a fully plastic or elastic-plastic deformation field.

Crack propagation occurs as a mixture of three limiting modes, as shown in Figure 6.1. Mode I crack propagation is associated with in-plane tension, Mode II is associated with in-plane shear, and Mode III is associated with out-of-plane shear. Actual crack propagation is rarely so distinct (e.g. slant fracture consisting of Modes I and III can be caused simply by Mode I loading). As one could imagine tearing a page out of a telephone book, the metal plating will be opened by in-plane tension and torn by out-of-plane shear. Crack propagation from the rough edge of a hole in a thin shell will be caused primarily by slant fracture.



## 6.2 Physical Basis of Plastic Fracture

A fully plastic situation consists of plane strain, plane stress, or intermediate modes which occur when the plastic zone is large relative to the plate thickness. The plastic zone will, for plane stress, become large and spread through the whole cracked section if the net section stress is of the order of the yield strength. In practice, linear elastic fracture mechanics (LEFM) does not apply if the fracture stress is greater than two-thirds of yield [40]. Plane stress requires the vanishing of one of the principal components of stress,  $\sigma_{zz}$ , and the vanishing of stress gradients in the  $z$  direction. Plane stress occurs when the out-of-plane dimension is far thinner than that required for plane strain, as in a thin plate or shell.

The tearing of thin sheets of ductile metals is a process of combined flow and fracture. Plasticity precedes and accompanies crack propagation. Necking may occur when the plastic zone size becomes larger than the plate thickness. Stress and strain distributions in the region of the tip of a sharp crack are complex. Stress changes are very large within one plate thickness of the crack tip, and a state of plane strain may be approached. Plane stress behavior will be exhibited beyond roughly four plate thicknesses of the crack tip [10].

Crack propagation can be regarded as a process of hole nucleation, coalescence, growth, and localization. Localization may occur first in plane stress. Tipper [41] examined sections near the fracture surface cut from different mild steel specimens. In ductile steels, hole nucleation almost certainly occurs by the drawing away of the metal from non-metallic inclusions. Separation of the metal around inclusions occurs at some distance (1 or 2 hole spacings) ahead of the crack tip,



and may occur with stresses as low as yield. The holes become linked by elongation and eventually produce macrofracture.

### 6.3 Analytic Approaches to Plastic Fracture

Plastic fracture is a complex process whose mechanisms are not fully understood. These mechanisms include hole nucleation, coalescence, growth, and localization of plastic flow into bands. Linear and non-linear elastic fracture mechanics are relatively well understood for crack initiation in plane strain, but do not apply to the loading of shells and subsequent crack growth. Despite considerable research within the last ten years, according to Broek [40], no generally accepted approach to elastic-plastic fracture mechanics (EPFM) has been developed. Kardomateas and McClintock [42] indicate that ductile fracture occurs by hole growth, which depends on the combined history of strain, stress, and rotation near the crack tip. Fully plastic fracture mechanics (FPFM) can thus not be described by a single measure of failure.

Several promising approaches to EPFM are being developed, however, which offer some insights into the process. These approaches generally consist of either a stress field analysis or an approximate global energy analysis. A stress field approach examines the stress field around the crack tip, as the K factor does in LEFM. An energy approach examines the energy release associated with crack initiation. Both approaches, unfortunately, have their limitations.

Although it has not been accepted as a universal fracture criterion, the J-integral provides a means to determine an energy release rate for both LEFM and cases where plasticity effects are not



negligible [40]. The J-integral is defined along a contour around the crack tip as the change in potential energy for a virtual crack extension. The U.S. Navy has adopted a J-based approach to fracture toughness characterizations of ductile materials [43]. In general, though, the J-integral is unable to handle large amounts of stable crack growth accompanied by full plasticity because unloading occurs along a different stress-strain curve than during loading, and also because of differing degrees of triaxiality with different geometries and low hardening. McClintock [10] further emphasizes that an energy approach to plastic crack propagation is global in nature and can not account for the different fracture process zone stress-strain distributions and the local mechanisms of crack growth. Crack initiation, however, is an especially local phenomenon and can be adequately described by an energy approach.

Atkins [44] has developed a rigid-plastic fracture analysis which reasonably accounts for and simplifies the complex nature of fully plastic fracture (FPFM) in certain situations. In this approach, the relative magnitude of flow and fracture components is an important factor in determining the transition from plastic flow preceeding fracture to crack initiation and propagation. Although this approach is limited by its global nature, it offers a useful engineering analysis of FPFM, and is presented because of its promise.

A limit load analysis offers a new approach to the problem of fully plastic crack propagation. By selecting realistic displacement fields it may be possible to define what loads cause deformation which could tend to promote crack propagation.





#### 6.4 Rigid-Plastic Fracture Analysis

A rigid-plastic simplification of EPFM may be applied to a variety of sheet tearing problems. Plastic fracture involves remote flow, which Atkins [44] incorporated into an expanded quasi-static elastic fracture energy equation in terms of the elastic strain energy  $\Lambda$ , the fracture toughness or specific (essential) work of fracture  $R$ , the total plastic work  $W^P$ , the residual strain energy  $\Lambda_r$ , and kinetic energy  $H$  as:

$$P \, du = d\Lambda + R \, dA + dW^P + d\Lambda_r + dH \quad (6.1)$$

where  $P$  is load,  $u$  is load-point displacement, and  $A$  is the crack area. In the specific case of dynamic tearing of ductile metal sheets the limiting crack speeds consistent with a quasi-static approximation are usually some 1 to 10 m/s [44]. The kinetic energy term may be equated to zero for most materials and cracked geometries. Cracks, whether surrounded by elastic or plastic fields, tend to propagate with their own crack opening angles. The rigid-plastic fracture equation can be further simplified in the case of extensive plastic flow, where it may be permissible to neglect  $d\Lambda$ , as:

$$P \, du = R \, dA + dW^P \quad (6.2)$$

This equation has found success in Cotterell and Mai's [45] studies of fracture in ductile sheets, and in Atkin's studies of metal forming fracture such as cropping and can opening. These studies demonstrated that geometry-independent  $R$  values do characterise the fracture behavior and that plastic flow and fracture terms may be separated in the rigid-plastic fracture equation. Atkins cautions, however, that fracture toughness may be path dependent according to a McClintock-type analysis.



Atkins and others have examined crack propagation due to various loading modes. Experiments by Mai and Cotterell [46] in which the bending and unbending plastic work could be altered independently of the fracture work gave roughly the same values for fracture toughness. The experiment used two metals (low alloy steel Lyten and a 5251 aluminum alloy) with different work hardening indices in both two and three leg "trouser" tests to alter the plastic work independently of the fracture work. This demonstrates that the flow and fracture work components can sometimes be uncoupled and that the toughness so determined is a material property, and indicates that the rigid-plastic equation is valid for certain applications.

From a global energy approach, crack propagation will occur if the combined flow and fracture associated with propagation requires a smaller work increment than flow alone. An increment of plastic flow may be written:

$$dW^P = d(\Gamma V) = \Gamma dV + V d\Gamma \quad (6.3)$$

where  $\Gamma$  is the total plastic work per unit volume and  $V$  is the volume undergoing plastic deformation. The plastic flow equation governs the external work required prior to fracture and applies with incremental changes  $dV$  and  $dW^P$  since there is new material entering the fracture process zone as crack propagation occurs. By considering increments of external work, and the additional work required to propagate cracks, Atkins was able to describe stable crack propagation as:

$$n = \frac{V}{R} \left[ \frac{d\Gamma}{dA} \right] \quad (6.4)$$

where  $n$  is the number of propagating splits [44]. The stability of



crack propagation is dependent upon boundary conditions and loading as limited by the structure's compliance.

This analysis was applied by Atkins [47] to the case of axial splitting of ductile metal tubes. The ends of the tubes were flared by being forced down onto conical mandrels, as shown in Figure 6.2. The number of starter cuts produced extremely interesting axial splitting behavior. With a small number of starter cuts, all cuts would propagate and some would bifurcate. With a larger number of starter cuts, some cuts would never develop into cracks. In all cases, the final number of propagating cracks was always between 8 and 12 for 50mm diameter and 1.6mm wall thickness mild steel and aluminum tubes. Crack propagation was a stable process with a reasonably constant radius and all the splits having equal lengths. Atkins applied geometry and experience to the incremental plastic flow analysis in order to derive the relationship:

$$n \cong (8\pi / \sqrt{3}) (\bar{\sigma} / R) r \epsilon_{\theta} \quad (6.5)$$

where  $\bar{\sigma}$  is the effective stress,  $r$  is the radius of the tube, and  $\epsilon_{\theta}$  is the average hoop strain. Atkins' method predicts  $n \cong 12$ , which indicates that the incremental plastic flow analysis can be successfully applied to some complex problems.

#### 6.5 Plastic Limit Load Fracture Analysis

Crack propagation is encouraged by transverse strain, and ensuing necking and hole nucleation, in front of the crack tip. These strains can be produced by certain displacement fields within a fully plastic structure. The limit load for a crack of given length, with necking



neglected, can be found by examining the simple case of vertical up and down cracks extending from a central circular hole in a flat plate.

An upper bound to the limit load is given by a displacement field which satisfies any displacement boundary conditions and gives no change in volume anywhere. The upper bound  $P_{ub}$  can be found from:

$$\delta W^P = P_{ub} \delta u^P = \int Y \delta \bar{\epsilon}^P \delta V \quad (6.6)$$

where  $W^P$  is the plastic work,  $u^P$  is the displacement under  $P_{ub}$  in its direction,  $Y$  is the flow strength,  $\bar{\epsilon}^P$  is the equivalent plastic strain, and  $V$  is the volume. Experience with the crushing of initially deformed structures suggested separating the displacement field into two zones, as shown in Figure 6.3. The Zone II displacement field reflects the dominant shear strain evident during testing which places the crack under tension. Plastic work is equal to the applied load multiplied by the displacement caused by plastic deformation of the structure. the total displacement of the edge experiencing uniform compressive loading in the direction of the applied load is composed of in-plane compression and drop due to deflection.

Plastic work is a function of stress and strain throughout the structure. For non-hardening plasticity, the plastic work occurs at the yield strength, which means that the flow strength  $Y$  can be considered equal to  $\sigma_y$ . Since it is assumed that the thickness remains essentially constant during deformation, Eq. 6.6 can be rewritten as:

$$W^P = \sigma_y h \iint \delta \bar{\epsilon}^P \partial x \partial y \quad (6.7)$$

The integral must be evaluated separately for both zones and then summed to find the upper bound to the limit load. The equations are simplified by defining a displacement ratio of the maximum vertical deflection to





the maximum horizontal deflection. Since the equivalent plastic strains for this case are so complex, the plastic work is solved using a numerical integration technique.

The results indicate that as the initial flare (dishing) angle increases the least upper bound decreases. Curves of normalized load versus displacement ratio for different initial angles of flare are presented in Figure 6.4. The normalized least upper bound decreases from 0.58 to 0.35 as the initial angle of flare increases from 0 to 45 degrees. The displacement ratio associated with the normalized least upper bound also decreases with increasing initial angle of flare.

Hodge [11] and Gordon and McCrum [12] performed uniform displacement limit load analyses of a flat square plate with a central circular hole of varying size, without any cracks. With a cutout ratio ( $c/b$ ) of 40 percent, Hodge predicts an upper bound of 0.53 and a lower bound of 0.41, and Gordon and McCrum predict an upper bound of 0.60 and a lower bound of 0.47. The author's analysis describes a least upper bound of 0.58 for such a case. A structure will only fail in the assumed mode involving crack propagation if it does not first fail at a lower applied load according to a different mechanism.

Although the author's approach is analytically correct, it does not provide any indication of the effect of an initial crack. It is not reasonable that structures will be unaffected by the presence of cracks, regardless of material properties. It seems likely that the least upper bound is too "loose," and that the displacement field needs to be improved. Further upper bound limit load analysis of fractures could be conducted using a displacement field which specifically incorporates thinning in front of the crack tip, different  $u$  and  $v$



displacement fields, and various hole and crack sizes. Crack propagation is promoted by a displacement field which produces a combination of strain and triaxial stress in front of the crack. A fracture criterion could then be assumed in the form of crack growth per unit thinning or displacement across the crack tip.

#### 6.6 Crack Propagation from a Circular Hole

Crack propagation from a centrally located circular hole in a thin shell is a very complex problem. A J-based approach does not seem appropriate, Atkins' incremental plastic flow analysis can not be readily applied, and a limit load analysis does not provide significant illumination of the problem. Further research is required in the field of fully plastic crack propagation.



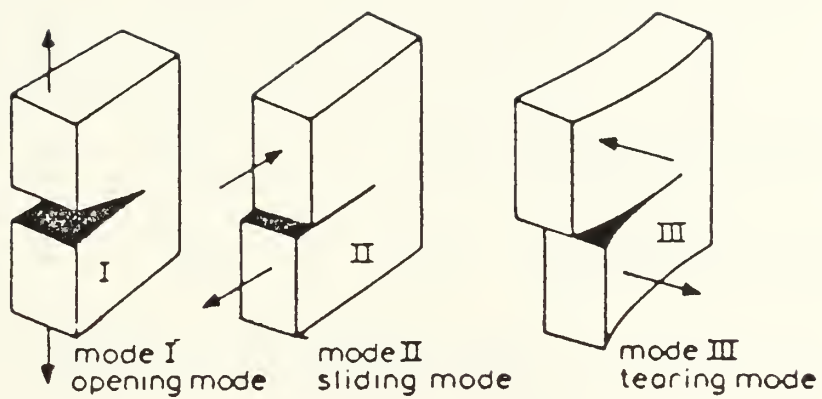


Figure 6.1: The three modes of loading which lead to crack growth [40]

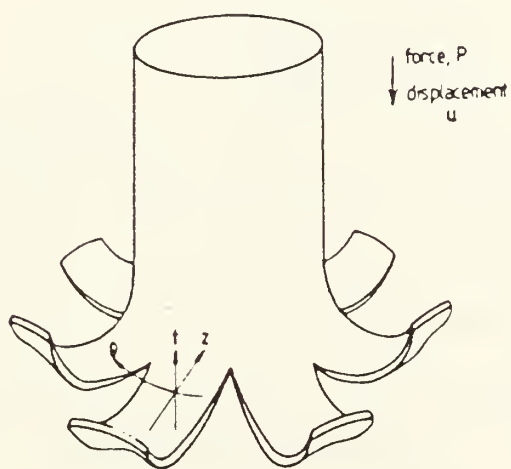


Figure 6.2: Axial splitting of ductile metal tube [47]



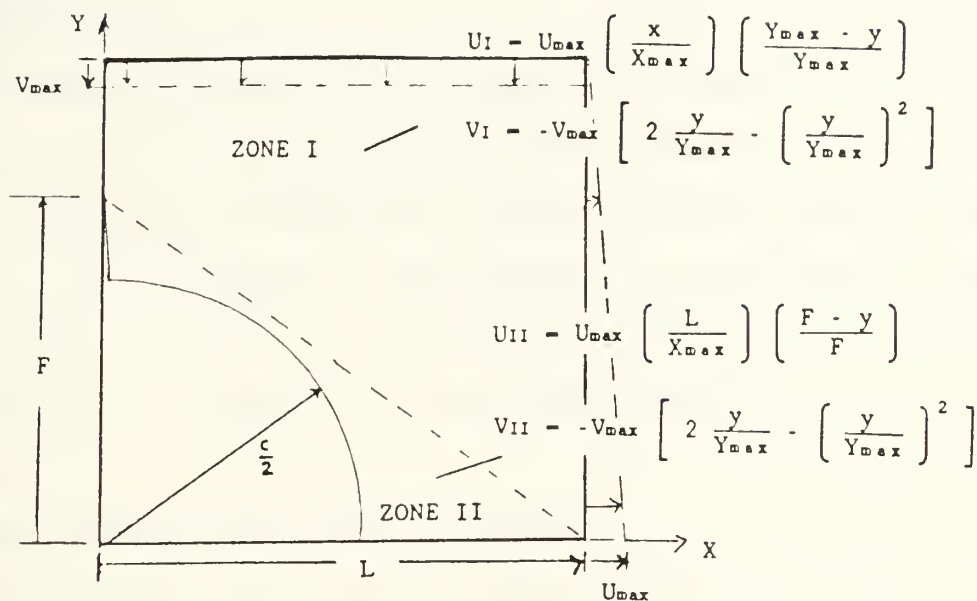


Figure 6.3: Quadrant of damaged plate and assumed displacement fields

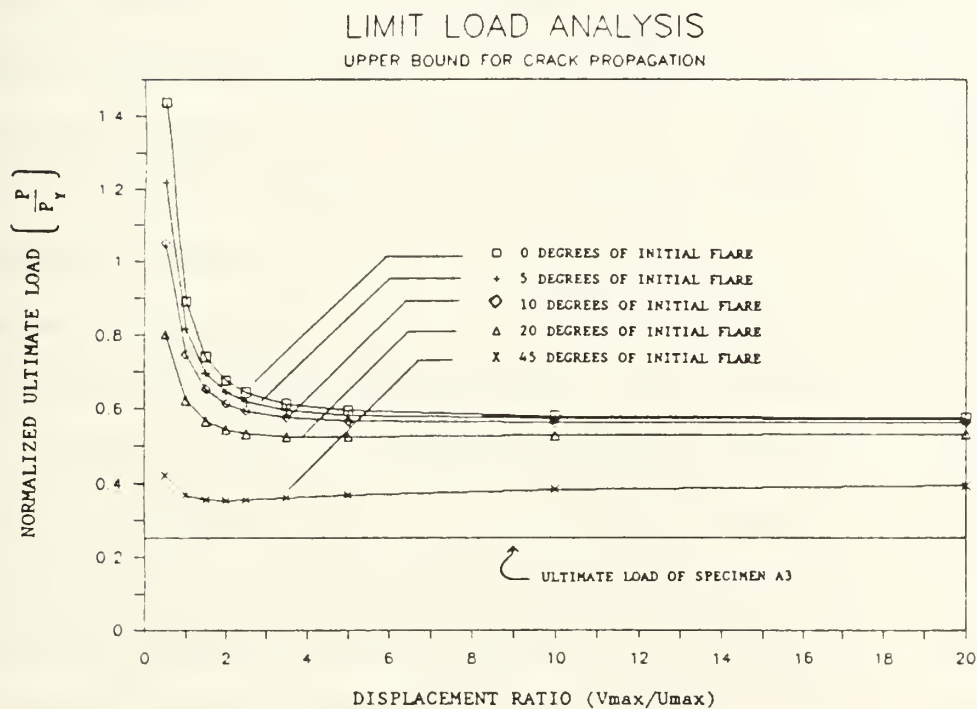


Figure 6.4: Graph of upper bound limit load versus displacement ratio for different initial angles of flare (dishing)





## 7. EXPERIMENTS AND DISCUSSION

### 7.1 Introduction

An internal airblast produces a variety of damage modes examined in this paper. The combined structural effects of damage, which consist primarily of holing, dishing and tearing, have not been previously studied. A small program of experimentation, consisting of crushing seven different specimens, was therefore developed to gain qualitative insights into the interaction of various damage modes.

### 7.2 Cumulative Structural Effect of Damage

By considering the individual damage effects as a whole it is possible to paint a picture of the residual strength of structural plating within a ship's compartment after an internal explosion. Plastic limit load analysis of a flat plate indicates that ultimate strength decreases in proportion to increasing hole size. Elastic-plastic buckling and post-buckling analysis indicates that ultimate strength is little affected by hole size until the holing reaches half the plate width, and is essentially equal to the peak load defined by the effective width concept. The dishing of a flat plate by an explosive loading is related to impulse and plate geometry and material properties. An extension of the concept of small initial imperfections to a dished plate suggests that the ultimate strength is reduced by roughly 10 percent from that of a flat plate. Finally, the extensional collapse mode analysis indicates that the mean crushing load of shipboard structural plating is roughly 0.1 of the tensile yield load. Although the mean crushing load decreases with increasing hole



size, it is suggested that it is relatively unaffected by the extent of initial dishing. Fully plastic crack propagation has been examined, but its limiting effect can not be precisely described. Warship design incorporates the use of ductile structural plating and crack arrestors to negate the effect of initial cracks upon residual strength.

Disregarding the potential effect of crack propagation, the theoretical combined effect of damage is shown in Figure 7.1 for shipboard structural plating with a length-to-thickness ratio of 250. Ultimate strength is described by the elastic-plastic out-of-plane failure mode presented in Chapter 3. The plastic in-plane failure mode, presented in Chapter 2, does not limit the peak load. Large-scale dishing, on the order of 5 to 10 plate thicknesses from explosive impulse, only reduces the ultimate load of an unperforated plate by 10 percent. Following peak load, the mean crushing load ranges from 0.06 to 0.13 for an unperforated plate, as presented in Chapter 5. Both ultimate and mean crushing strength are little affected by small holes (less than half the width). While the cumulative effect of damage can significantly reduce the residual strength of structural plating, the plating retains roughly 40 to 50 percent of its original strength. The residual strength, even with extensive damage, is improved by support members which continue to provide clamped edge boundary conditions to structural plating. The compliance of the ship tends to restrict extensive crushing and provides support to the plating to allow it to continue to support normal service loads.

### 7.3 Experimental Method

Although not an exhaustive study, the experimentation was designed



to examine the impacts of different failure modes of damaged structure, and validate the analysis summarized in Chapter 7.2. The theoretical analysis is concerned with the case of an initially flat square plate. The simplest way to perform a uniaxial compressive loading of the plate was to construct a symmetrical box with four square side plates and two stiffened end plates. This arrangement produced a "natural" boundary condition at the side plate edges which maintained their right angle relationship during initial yielding, but did not prevent out-of-plane deformations. The side plates were essentially clamped at top and bottom and simply supported at the unloaded edges.

A baseline "undamaged" specimen was built of four undeflected side plates. Two basic specimen types were designed to reflect different possible modes of lateral deflection produced by the airblast, as shown in Figure 7.2. In order to model the different possible modes of dishing (lateral deflection) from the initial undamaged condition, edge pieces were cut slightly larger and bent to shape such that the base dimensions and height of each specimen maintained the initial dimensions. Type A specimens represent an "Accordion bulge" which has caused the edges of the plate to deflect along with the center. Type B specimens represent a "Basketball bulge" which has not deflected the edges of the plate. Due to geometrical constraints of the supplied metal, Type A specimens were built with a peak deflection-to-thickness ratio of only 3.9, while the Type B specimens were built with a peak deflection-to-thickness ratio of 12.9. Three specimens were built of each type, with a central circular hole on all faces.

The specimens were built of 1/16 inch thick mild steel (ASTM A-515 grade 70) plates welded together by the TIG method. The standard ASTM



characteristics for this steel are presented in Table 7.1. The U.S. Navy uses ASTM A-515 grade 70 steel in construction of Navy boiler drums and headers. During fracture mechanics tests performed by the Navy, this carbon steel underwent substantial non-linear deformation followed by cleavage. It is in fracture mode transition at room temperature [48]. The U.S. Navy has recently adopted HSLA-80 (ASTM A-710 grade A-class 1 is typical) steel for use as structural plating in the hull and superstructure of warships. The standard ASTM characteristics for this micro-alloyed, fine-grain, low-carbon steel (as rolled and precipitation heat treated) are also presented in Table 7.1.

Table 7.1: Tensile properties of ASTM A-515 grade 70 mild steel and ASTM-710 grade A-class 1 low-carbon steel [49]

A-515 mild steel		
Composition (%)	C < 0.27 , Mg 0.79-1.30 P < 0.035 , S < 0.04 Si 0.13-0.45	
$\sigma_{UTS}$ , Ultimate Tensile Strength	70-90 ksi [485-620MPa]	
$\sigma_y$ , Yield Strength	38 ksi [260 MPa]	
Maximum Thickness	8 in	[200 mm]
A-710 HSLA steel		
Composition (%)	C < 0.07 , Mg 0.40-0.70 P < 0.025 , S < 0.025 Si < 0.4 , Ni 0.7-1.0	
$\sigma_{UTS}$ , Ultimate Tensile Strength	90 ksi	(655 MPa)
$\sigma_y$ , Yield Strength	80-85 ksi	(550-585 MPa)
Maximum Thickness	3/4 in	(20 mm)

Hardness testing (Rockwell 30T) of the as-rolled specimen material yielded Knoop numbers ranging from 112 to 120 kg/mm<sup>2</sup>. Empirical analysis of these values indicated that the specimen material is softer





than that specified by ASTM characteristics. Since accurate tests of the yield strength were not conducted, however, the tensile yield load  $P_y$  for the specimens was calculated with the specified yield strength value of 38 ksi.

The initial undeflected square plate had dimensions of 5.5 by 5.5 inches (140 by 140mm), for a length-to-thickness ratio of 90. A warship's structural plating has a length-to-thickness ratio, neglecting stiffeners, on the order of 200 to 300. Economic and time limitations dictated the selection of A-515 mild steel for constructing the specimens. Although this is a good ductile steel to represent the performance of HY-80 and HSLA-80 used in U.S. Navy warships, the specimens were relatively thicker and softer than actual structural plating.

A simple undamaged specimen was crushed to serve as a baseline for comparison purposes. The first set of tests consisted of a specimen of each type, labeled A1 and B1 respectively, with the lateral deformation pattern unique to each. Specimens A1 and B1 had a 2-1/4 inch (57mm) central circular hole on all side plates, which represented a cutout ratio (c/b) of 41 percent. The second set of tests was similar to the first, but with the addition of a rosette of 8 cracks, 1/2 inch (12.6 mm) long radiating from each hole, and labelled A2 and B2. The holes in specimens A2 and B2 were the same size as in the first set of specimens. Crack tips were cut with hack-saw blades which had their sides ground down to ensure good initial notches for crack growth. The third set of tests was designed to evaluate the effects of changing hole size and initial crack formation. Specimen A3 had the same hole size as previous specimens, but was modified with a set of short 1/4 inch (6mm) vertical



cracks radiating from each hole. Specimen B3 was modified with a larger central circular hole of 3-3/8 inches (86mm), which represented a cutout of 61 percent, but had no initial cracks. Table 7.2 presents a tabulation of the initial conditions of the various specimens. The six "damaged" specimens represented a variety of initial damage effects.

Table 7.2: Initial structural condition for all specimens

Specimen	Baseline Un- damaged	Type A (Accordion)			Type B (Basketball)		
		A1	A2	A3	B1	B2	B3
Dishing $\left(\frac{w_{cf}}{h}\right)$	0	3.9	3.9	3.9	12.9	12.9	12.9
Cutout $\left(\frac{c}{b}\right)$	0	0.41	0.41	0.41	0.41	0.41	0.61
Starter Cracks per Plate	0	0	8	2	0	8	0

The specimens were crushed on a Baldwin-Tate-Emery 60,000 psi machine to determine load versus displacement characteristics. The testing apparatus is shown in Figure 7.3. Uniform displacement was regulated by manual control of hydraulic flow. Load versus displacement data beyond ultimate load was only recorded by first unloading and then reloading slowly until the specimen resumed deflection. The testing machine had a nominal compliance of 1 inch per 200,000 lb. which was considered negligible for this experimentation. Loads were normalized with respect to the tensile yield load as described by Eq. 2.5:

$$P_Y = \sigma_Y A \quad (7.1)$$

and displacements were normalized with respect to the original specimen height. Specimens were crushed to 13 to 50 percent of their original



length.

#### 7.4 Experimental Results

All specimens exhibited generally similar elastic load-deflection curves, although ultimate strength and post-buckling behavior varied considerably. The original load-displacement data for all specimen crush tests is recorded in Appendix A. All of the specimens demonstrated linear elastic behavior during the initial loading. Loss of strength was generally rapid after the peak load was reached. With continued crushing, however, the strength of each specimen leveled off and then increased as local folding zones collapsed.

The baseline undamaged specimen supported a peak load of 20,600 lb. prior to collapsing, for a normalized ultimate load of 0.393. Normalized load versus displacement curves for all specimens are presented in Figures 7.4 and 7.5. The loads were normalized with respect to the tensile yield load  $P_y$ , and the deflections were normalized with respect to the original baseline dimensions. The first holed specimens, A1 and B1, supported normalized ultimate loads of 0.247 and 0.275 respectively. The buckling mode which developed in specimen B1 after the peak load was reached is shown in Figure 7.6. The second set of holed specimens with a rosette of cracks, A2 and B2, supported normalized ultimate loads of 0.223 and 0.280 respectively. Only specimen A2 experienced crack propagation. The crack growth occurred only after the crack tips had been re-notched to eliminate the bluntness which had developed during the initial loading and after extensive crushing beyond the peak load. The buckling mode which developed in Specimen A2 after the peak load was reached is shown in Figure 7.7. The



limited crack propagation which developed was primarily Mode III tearing as shown in Figure 7.8. Specimen A3, with short vertical cracks, only supported a normalized ultimate load of 0.253. Although pinching (necking) was observed at the crack tips, specimen A3 experienced no crack propagation. Specimen B3, with larger circular holes, supported a normalized ultimate load of 0.248. The only visible weld failure occurred in specimen B3 during crushing beyond 40 percent of initial length. Table 7.3 presents a tabulation of the experimental results.

Table 7.3: Ultimate and mean crushing load  
experimental results for all specimens

Specimen	Baseline Un- damaged	Type A (Accordion)			Type B (Basketball)		
		A1	A2	A3	B1	B2	B3
Ultimate Load (lb.)	20060	12600	11400	12920	14060	14320	12680
Normalized Ultimate Load	0.393	0.247	0.223	0.253	0.275	0.280	0.248
Mean Crushing Load (lb.)	8700	9700	9200	9700	5600	5600	5600
Normalized Mean Crush Ld	0.17	0.19	0.18	0.19	0.11	0.11	0.11

## 7.5 Discussion of Results

The experimentation gives some insight into the loss of strength associated with damage. The cumulative analysis of damage effect failure modes is applied to the specimen side plates and summarized in Figure 7.9. The experimental results are also plotted in Figure 7.9 for comparison purposes. Out-of-plane buckling caused all of the specimens





to collapse at lower loads than the tensile yield load. The effect of damage can, perhaps, be best seen by comparing damaged specimen strength characteristics with the baseline undamaged specimen. Although the experimentation consisted of just seven specimens, some trends or observations can be made about each of the different damage effects.

Boundary conditions affect the plate buckling mode and strength characteristics. Figure 7.10 shows how the plate buckling coefficient  $K$ , which is directly related to the plate critical load, is affected by boundary conditions. The actual boundary conditions imposed upon the specimen side plates is illustrated by the clamped loaded edges - C condition shown in Figure 7.10. The plastic limit load and elastic-plastic analyses presented in Chapters 2 and 3 only examined simply supported edge boundary conditions. The critical buckling curve, shown in Figures 5.2 and 5.3, indicates that buckling of slender square plates of baseline specimen dimensions occurs at roughly 40 percent of peak load. Although the actual boundary conditions of the specimen plates should have given the plates greater strength than predicted analytically, out-of-plane buckling and peak load for the baseline and damaged specimens occurred at lower loads.

All experimental results for ultimate and mean crushing load lie below the analytic solutions, as shown in Figure 7.9. Since the analytic solution for ultimate strength of an unperforated flat plate is known to be reliable, it seems likely that the low normalized ultimate strength for the baseline specimen was produced by using too high a yield strength value to determine the tensile yield load. Hardness testing indicated that the specimen material was softer than specified. A lower yield strength of 30 ksi brings the normalized experimental



results into line with the analytic solutions. Since the true yield strength is not known, however, it is useful to compare the results of crushing the damaged specimens with the baseline specimen.

Increased holing clearly reduces residual strength. The behavior of specimens B1 and B3 during crushing describes the effect of increased holing. As the cutout ratio increased from 41 to 61 percent, with other initial damage effects constant, the normalized ultimate load decreased by roughly seven percent as compared to the baseline. These experimental results support the relative loss of strength with increased holing described by the elastic-plastic analysis. This indicates that although holing clearly reduces strength, it does not cause a rapid loss of strength.

Dishing produces a significant loss of strength. It clearly biases the buckling mode towards its own shape. The experimentation ignores the effect of actual thinning, which would be associated with dishing, upon strength. While the undamaged baseline specimen buckled asymmetrically (opposite sides folded in or out together), all damaged specimens buckled symmetrically with outward folds near mid-plate. Although the Type B specimens retained greater ultimate strength than the Type A specimens, their post-buckling mean crushing load was less. It seems reasonable that the Type B specimens retained greater ultimate strength because their edges were initially straight, while the Type A specimens were initially flared out. While the Type A specimens experienced horizontal folding along the mid-plane as predicted, the initial deflection (dished) shape of Type B specimens caused the folding zones to angle out from the central holes away from the mid-plane. In the post-buckling range, dished shape, holing, and slenderness may become



the dominant defining mean crushing load strength.

A tentative quantitative estimate on the effects of dishing alone can be made by extrapolation of the experimental results. Assuming a linear reduction of strength with increased hole size, the peak load results from crushing of specimens B1 and B3 can be extrapolated to determine the loss of strength caused by dishing with no hole. A specimen with extensive initial dishing would thus have suffered a 16 percent loss of strength from the baseline undamaged specimen, which is a slightly greater loss than predicted analytically. According to the elastic-plastic analysis, however, the results from crushing of specimens A1 and B1 essentially represent the loss of strength due to dishing alone. A specimen with extensive initial dishing, but no holing, would thus have suffered a 30 to 37 percent loss of strength from the baseline undamaged specimen. The effect of actual thinning of structural plating during dishing caused by an explosion is considered negligible. There is unfortunately no way to determine the validity of this approach, or to apply it to other dished mode shapes, from the limited experimental data.

Both initial hole size and deflection shape affect the mean crushing load. By assuming that the flow strength for A-515 mild steel equals 63 ksi, from Eq. 5.5 with  $\sigma_{uts} = 70$  ksi, it is possible to apply the extensional collapse mode analysis to the test specimens. The upper and lower bounds from the analysis describe a normalized mean crushing load ranging from 0.31 to 0.20, and from 0.24 to 0.17 for a specimen with a cutout ratio of 41 percent. The baseline undamaged specimen had a normalized mean crushing load of roughly 0.17 during crushing, which again suggests that the specimen material was softer than specified.



The extensional collapse mode analysis predicts a folding zone width of 1.03 inches for the baseline specimen, from Eq. 5.7, which compares favorably to the observed width. Although the baseline specimen experienced repeated asymmetric folding, the damaged specimens experienced only one major folding pattern associated with the initial dished shape. Type A and B specimens, with a 41 percent cutout ratio, experienced different mean crushing loads of roughly 0.19 and 0.10 respectively. Significant holing has the effect of allowing out-of-plane motion of the plating around the hole and thus reducing the amount of energy absorbed by extensional deformation of plate sections. The extensional collapse mode analysis does not describe a significant loss of mean crushing load with increased hole size until the cutout ratio exceeds roughly 60 percent, which is supported by the experimental results (specimen B3 versus B1). The initial angled folding zones associated with Type B specimen buckling reduced the range of folding (i.e. less than the complete folding presumed by the extensional collapse mode analysis). It is suggested that holing and dishing combined can reduce the mean crushing load by roughly one-third as the dissipation of work becomes essentially quasi-inextensional deformation of hinge lines.

Fracture is a potentially serious problem in any damaged structure, but was not a significant determining factor in the residual strength of the damaged specimens. The initial starter cuts seemed to have little effect upon strength, possibly because the fine cuts did not have any necking in front of the crack-tip as would have been present in natural fully plastic fracture. The presence of starter cracks had no consistent effect upon ultimate strength. The limited crack propagation





in specimen A2 was caused by tearing associated with complete folding and subsequent contact of buckles produced by extensive crushing. The mean crushing strength of the specimens was little affected by the presence of starter cuts. The thinning in front of the crack-tips indicate that transverse tensile strains were present, but insufficient to promote crack propagation.

A ship's structural plating is relatively thinner and harder than the specimen side plates, and may experience quasi-static fracture more easily than the specimens did during testing. Fully plastic fracture in complex structures can not be described by current analytic techniques. Warship design, however, incorporates the use ductile materials to inhibit fracture, and stringers to serve as crack arrestors which limit any crack propagation.

It is difficult to determine the comparative effects of damage between holing, dishing and cracking. The range of experimentation only covered two different damaged mode shapes, two hole sizes, and two crack patterns, as described in Table 7.2. Although further experimentation is required to quantify the individual and cumulative damage effects, it is possible to apply the lessons learned from this research.

#### 7.6 Residual Strength of a Warship After an Internal Explosion

The DDG-51 Arleigh Burke Class destroyer is one of the U.S. Navy's most modern warships. The most demanding loading any ship generally experiences is located at its mid-section due to hogging and sagging conditions produced by the ocean. The DDG-51 is designed for a maximum hogging moment of 176,953 ft-tons and a maximum sagging moment of 87,883 ft-tons [50]. The maximum compressive loading condition of



4.2 tons/in<sup>2</sup> on the midships deck plating occurs during sagging.

From a structural standpoint, the worst single antiship missile hit would be one which produces an internal explosion amidships. An internal airblast between frames 220 and 254, from a small antiship missile such as the EXOCET, could easily produce a hole with a cutout ratio of 50 percent and dishing on the order of 10 plate thicknesses. In terms of longitudinal strength, the deck plating above the damaged compartment can roughly be considered a 10 by 10 foot square plate of 3/8 inch thick low-carbon steel. The worst condition sagging produces a load of 378,000 lb. on the plating, for a normalized load of 0.105. From the effective width concept, the undamaged structural plating can support a normalized ultimate load of 0.115, neglecting the positive effect of support members. Based upon the theoretical and experimental analysis presented in this paper, the ultimate strength of the damaged structure would be decreased by roughly 25 percent due to dishing and 5 percent due to holing, for a normalized ultimate load of roughly 0.08. The normalized mean crushing load, incorporating the effect of holing but neglecting dishing, would range from roughly 0.07 to 0.04. These strength characteristics indicate that the plating can not support extreme sagging conditions prior to ultimate load on its own, but could probably continue to support normal service loads before and after peak load. A local failure of the structural plating in one or more compartments does not mean that the ship will experience global failure. The ship's support members and structural compliance would offer continued support to the plating to prevent local collapse.



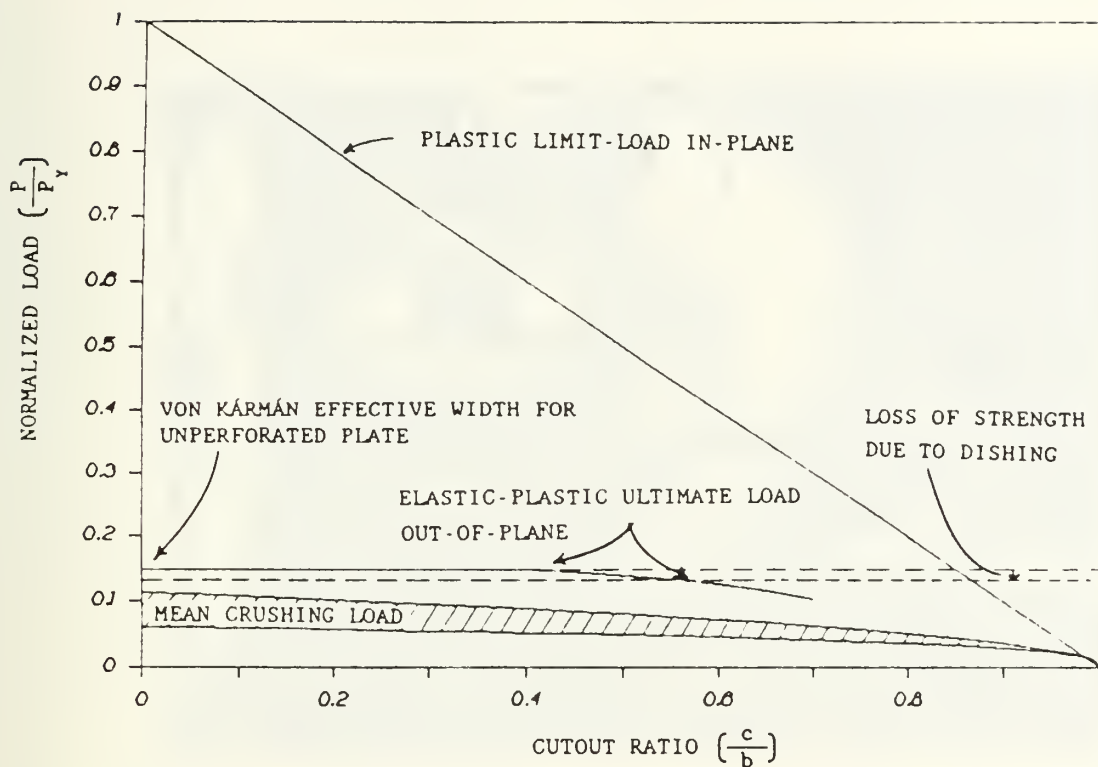


Figure 7.1: Summary of damage effect failure modes for shipboard structural plating with a length-to-thickness ratio of 250

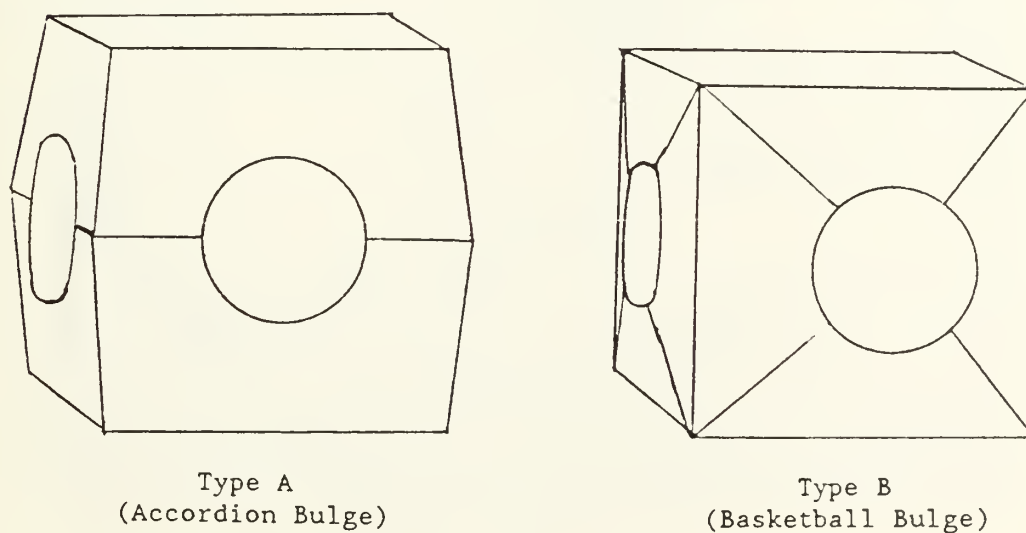


Figure 7.2: Specimen types with different simplified dishing (lateral deflection) modes



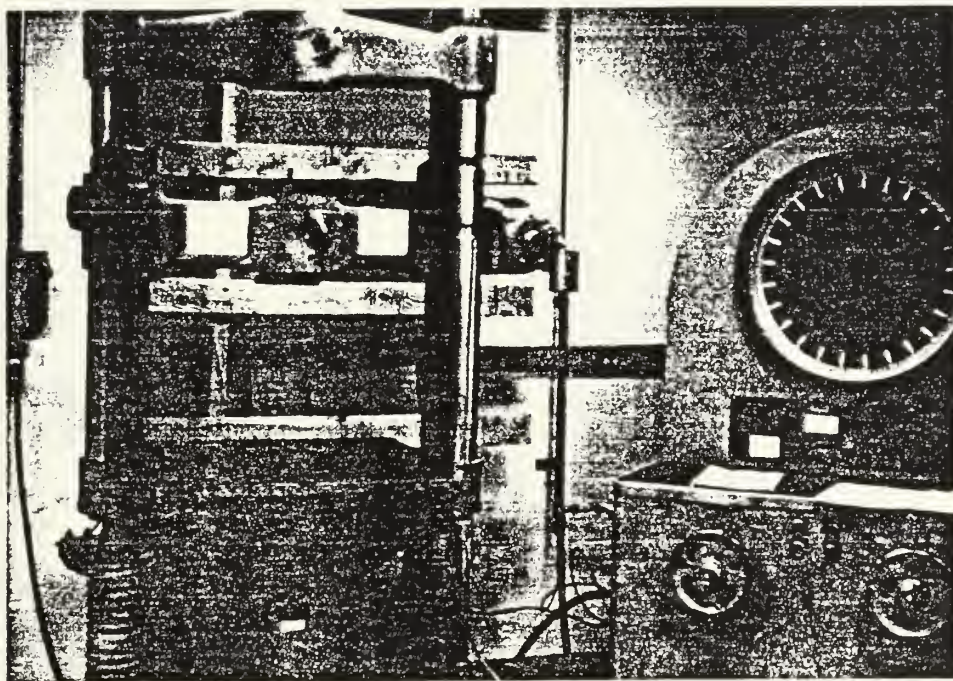


Figure 7.3: Photograph of testing apparatus

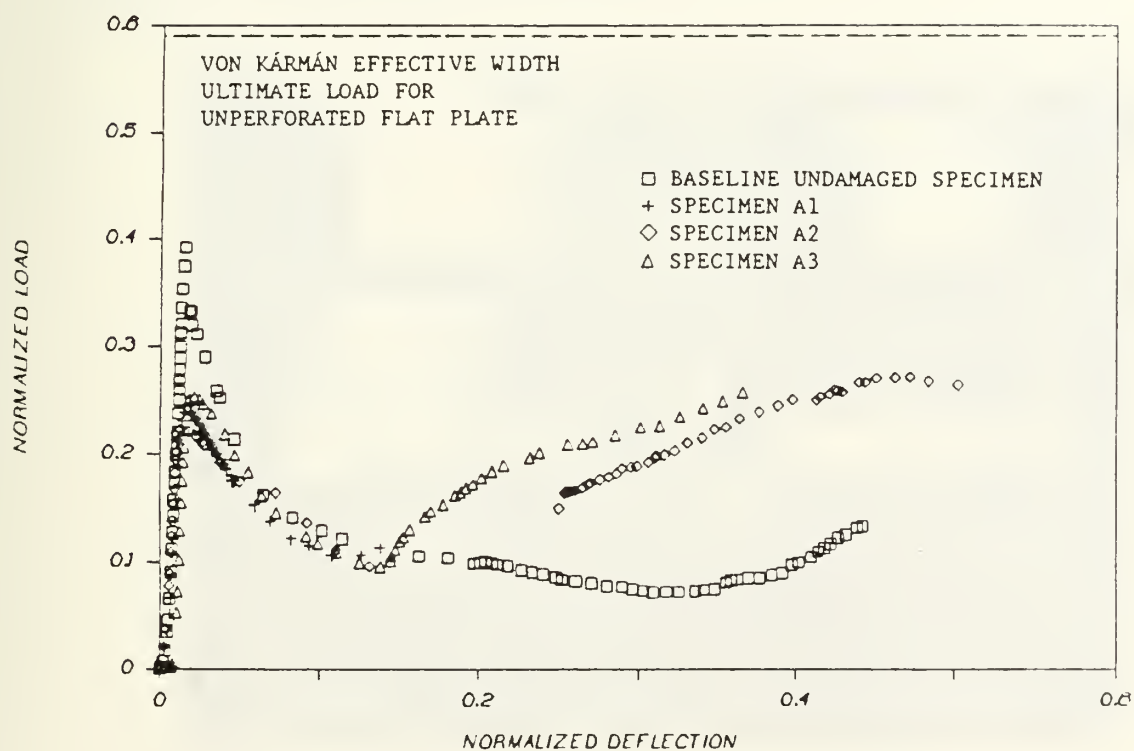


Figure 7.4: Graph of normalized load versus deflection for baseline and Type A (Accordion bulge) specimens





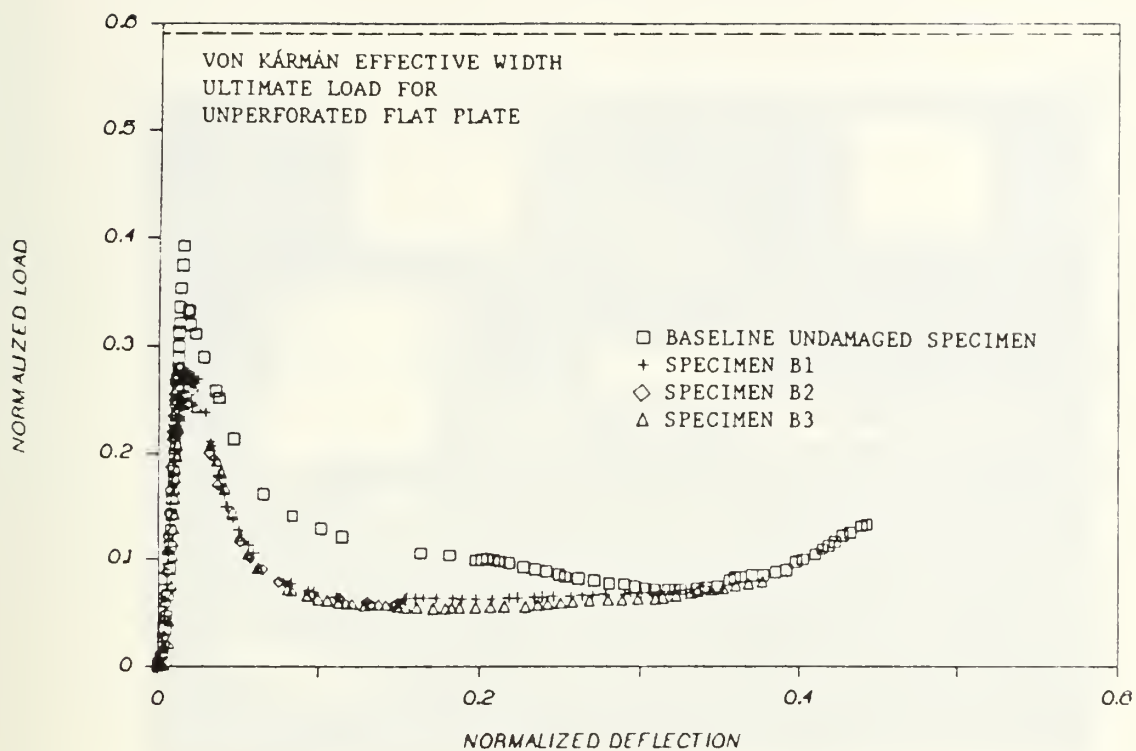


Figure 7.5: Graph of normalized load versus deflection for baseline and Type B (Basketball bulge) specimens

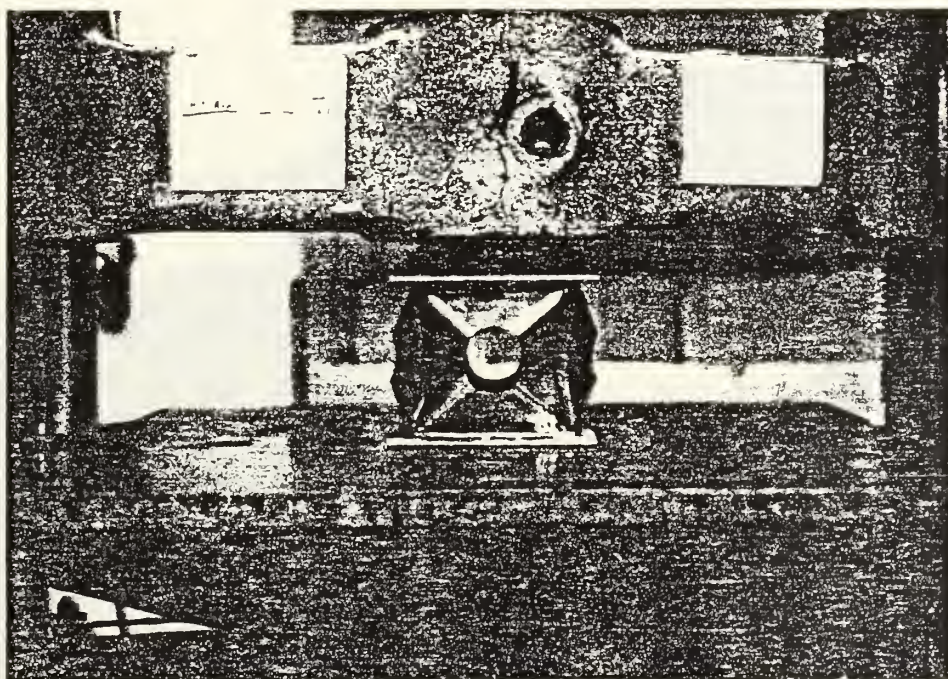


Figure 7.6: Photograph of specimen B1 shortly after ultimate load was reached





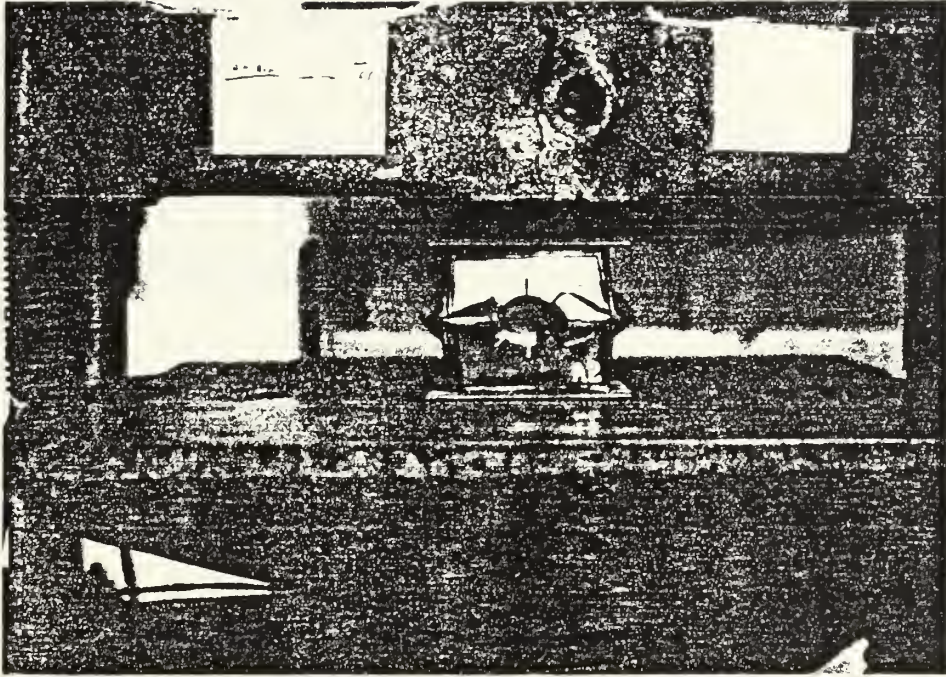


Figure 7.7: Photograph of specimen A2 shortly after ultimate load was reached

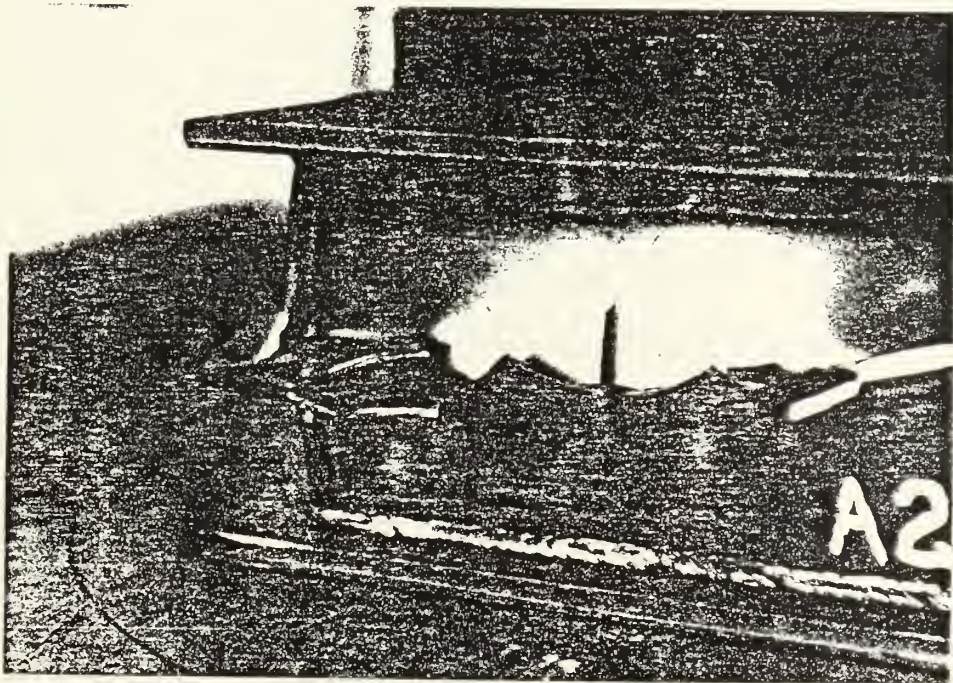


Figure 7.8: Photograph of tearing from a starter crack in specimen A2



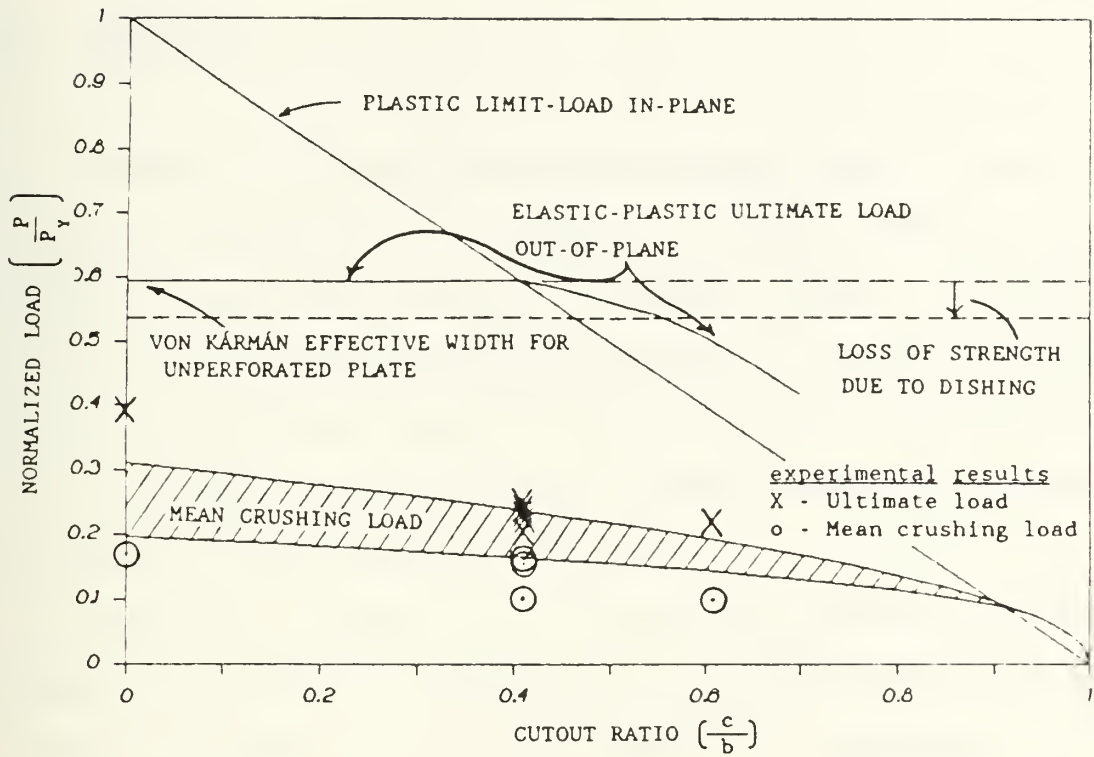


Figure 7.9: Summary of damage effect failure modes and experimental results for Gspecimen side plates with a length-to-thickness ratio of 90

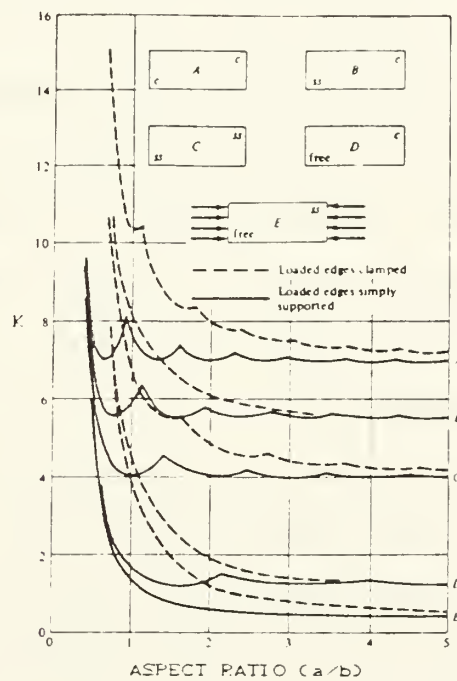


Figure 7.10: Graph of plate buckling coefficient versus aspect ratio for different boundary conditions [18]





## 8. CONCLUSION

Shipboard structural plating can continue to support normal service loading even after extensive damage. An internal explosion produces tearing, holing, and dishing of structural plating. The shipboard structure and damage effects were simplified in this paper in order to analyze the individual damage effects and determine how they interact. A small program of experimentation roughly validated the cumulative analysis of damage effect failure modes.

Structural collapse is a function of mechanical properties, structural geometry, and collapse mode. (1) The ultimate strength of structural plating is strongly affected by slenderness. (2) The elastic-plastic analysis accurately describes the ultimate load for slender plates, and indicates that small holes (cutout ratio less than 50 percent) have little affect. (3) Dishing on the order of 5 to 15 plate thicknesses reduces ultimate strength by roughly 15 to 35 percent. (4) The buckling mode involves folding as decribed by the extensional collapse mode analysis. (5) The normalized mean crushing load, which describes the average compressive strength maintained after the ultimate load has been reached, is roughly 0.1 for undamaged shipboard structural plating, and ranges from 0.05 to 0.1 for significantly damaged plating. (6) Although crack propagation was limited during crushing of the damaged specimens, fully plastic fracture could be more significant in shipboard structural plating. Continued reserach is required to further quantify these conclusions and apply the results to improved ship designs.





### 8.1 Ideas for Continued Research

This paper has presented the first qualitative theoretical and empirical analysis of the cumulative effect of damage upon structural plating. There are many avenues of continued research required to develop a comprehensive quantitative understanding of damage effects. Ideas for further research include: (1) determine the effect of ship's compliance upon plate boundary conditions, (2) determine the effect of stiffeners upon various damage modes, (3) investigate rectangular plate geometries, (4) determine the deflection of supporting members associated with plate geometries, (5) examine dynamic effects, (6) examine fully plastic fracture, (7) conduct extensive critical experimentation to determine quantitative relationship between damage effects. It is important that any testing properly model shipboard structural geometry (such as  $b/h$ ) and material characteristics (such as  $\sigma_y/E$ ). The author suggests that determining the effects of fully plastic fracture and shipboard structural compliance are particularly important.



## REFERENCES

1. U.S., Department of the Navy, Conventional Airblast (Contact and Internal), DDS-072, draft dtd 1 Apr 86.
2. Korotkin, I.M., Battle Damage to Surface Ships During World War II, trans. U.S. Joint Publications Research Service, Department of the Navy, Feb 1964.
3. U.S., Department of the Navy, Structural Survivability of Surface Ships, presented at ASNE Symposium, Pascagoula, Miss., NAVSEA 55Y dtd 24 Apr 86.
4. Layton, P.B., "Needed: A Better Antiship Missile Warhead," Proceedings, Vol.113, June 1987, pp.105-107.
5. U.S., Department of the Navy, Survivability Review Group Report on Surface Ship Design Principles, NAVSEA Tech Report 072-55X-TR-0005, Feb 1987.
6. U.S., Department of Defense, Introduction to Weapon Effects for Ships, DOD-HDBK-XX31CSH, draft dtd 15 June 1987.
7. Hiddemen, R.L., "Analysis of the Failure Mechanism of Shipboard Structural Members Exposed to Fire," Diss. Massachusetts Institute of Technology, June 1984.
8. Faulkner, D., "Compression Strength of Welded Grillages," in Ship Structural Design Concepts, edited by J.H. Evans, Cornell Maritime Press, Inc., Cambridge, Maryland, 1975, pp. 633-712.
9. Roberts, T.M. and Azizian, Z.G., "Strength of Perforated Plates Subjected to In-plane Loading," Thin-Walled Structures, Vol. 2, 1984, pp. 153-164.
10. McClintock, F.A., "Plasticity Aspects of Fracture," in Fracture an Advanced Treatise, Volume III, edited by H. Liebowitz, Academic Press, New York, 1971, pp.47-225.
11. Hodge, Philip, Plastic Analysis of Structures, McGraw-Hill Book Co., New York, 1959.
12. Gaydon, F.A. and McCrum, A.W., "A Theoretical Investigation of the Yield Point Loading of a Square Plate with a Central Circular Hole," Journal of the Mechanics and Physics of Solids, Vol. 2, 1954, pp. 156-169.



13. Gaydon, F.A., "On the Yield Point Loading of a Square Plate with a Concentric Circular Hole," *Journal of the Mechanics and Physics of Solids*, Vol.2, 1964, pp.170-176.
14. Prager, William, An Introduction to Plasticity, Addison-Wesley Publishing Co., Reading, Mass., 1959.
15. Kurshin, L.M. and Matveev, K.A., "Analysis of the Stability of Rectangular Plates with Holes," *Izv. AN SSSR. MTT [Mechanics of Solids]*, no. 6, 1978.
16. Ritchie, D. and Rhodes, J., "Buckling and Post- Buckling Behavior of Plates with Holes," *Aeronautical Quarterly*, Vol.26, No.4, 1975, pp.281-296.
17. Dubas, P. and Gehri, E., ed., Behavior and Design of Steel Plated Structures, Applied Statics and Steel Structures Swiss Federal Institute of Technology, Zürich, Switzerland, 1986.
18. Brush, Don O. and Almroth, Bo O., Buckling of Bars, Plates, and Shells, McGraw-Hill Book Co., New York, 1975.
19. Rhodes, J. and Harvey, J.M., "The Post-Buckling Behavior of Thin Flat Plates in Compression with the Unloaded Edges Elastically Restrained Against Rotation," *Journal of Mechanical Engineering Science*, Vol. 13, 1971, p.2.
20. Timoshenko, S.P. and Gere, J.M., Theory of Elastic Stability, 2nd Edition, McGraw-Hill Book Co., New York, 1961.
21. Jones, N., "Impulsive Loading of a Simply Supported Circular Rigid-Plastic Plate," *Journal of Applied Mechanics*, Vol.35, Mar 1968, pp.59-65.
22. Symonds, P.S. and Wierzbicki, T., "Membrane Mode Solution for Impulsively Loaded Circular Plates," *Journal of Applied Mechanics*, Vol.46, 1979, pp.58-64.
23. Nurick, G.N., "Large Deformations of Thin Plates Subjected to Impulsive Loading," *Diss. University of Capetown*, 1987.
24. Perrone, N. and Bhadra, P., "A Simplified Method to Account for Plastic Rate Sensitivity with Large Deformations," *Journal of Applied Mechanics*, Vol.46, 1979, pp.811-816.



25. Weibull, Hans R.W., "Pressures Recorded in Partially Closed Chambers at Explosion of TNT Charges," *Annals of NY Academy of Sciences*, Vol.152, 1968, pp.357-361.
26. Bodner, S.R. and Symonds, P.S., "Experiments on Viscoplastic Response of Circular Plates to Impulsive Loading," *Journal of Mechanics and Physics of Solids*, Vol.27, 1979, pp.91-113.
27. Manjoine, M.J., "Influence of Rate of Strain and Temperature on Yield Stress of Mild Steel," *Journal of Applied Mechanics*, Dec 1944, pp.211-218.
28. Lippman, H., "Kinetics of the Axisymmetric Rigid Plastic Membrane Supplied to Initial Impact," *International Journal of Mechanical Science*, Vol.16, 1974, pp.297-303.
29. Perrone, N. and Bhadra, P., "Simplified Large Deflection Mode Solutions for Impulsively Loaded Viscoplastic Circular Membranes," *Journal of Applied Mechanics*, Vol.51, 1984, pp.505-509.
30. Baker, W.E., "Approximate Techniques for Plastic Deformation of Structures Under Impulsive Loading," *Shock and Vibration Digest*, Vol.7 No.7, 1975, pp.107-117.
31. Johnson, W., Impact Strength of Materials, Crane - Russak, New York, 1972.
32. Frieze, P.A., Dowling, P.J. and Hobbs, R.E., "Ultimate Load Behavior of Plates in Compression," Steel Plated Structures, edited by P.J. Dowling et al., Crosby Lockwood Staples, London, 1976, pp.24-50.
33. Fujita, Y. and Yoshida, K., "On Ultimate Collapse of Ship Structures - Research in Japan," Steel Plated Structures, pp.542-558.
34. Scheer, J. and Nölke, H., "The Background to the Future German Plate Buckling Design Rules," Steel Plated Structures, pp.503-523.
35. Ueda, Y. et al., "Ultimate Strength of Square Plates Subjected to Compression (1st report)," *Journal of the Society of Naval Architects of Japan*, Vo.137, June 1975, pp.210-221, as reported in Y. Fujita and K. Yoshida, Steel Plated Structures, pp.542-558.
36. Minorsky, V.V., "An Analysis of Ship Collisions with reference to Nuclear Power Plants," *Journal of Ship Research*, Vol.3, 1959, pp.1-4.





37. Hayduk, Robert J. and Wierzbicki, Tomasz, "*Extensional Collapse Modes of Structural Members*," Computers and Structures, Vol.18, No.3, 1984, pp.447-458.

38. Wierzbicki, T. and Abramowicz, W., "*On the Crushing Strength of Thin-Walled Structures*," Department of Ocean Engineering, MIT, Technical Report 82-4 (April 1982).

39. Amdahl, J., Energy Absorption in Ship-Platform Impacts, Department of Marine Technology, the Norwegian Institute of Technology, the University of Trondheim, Trondheim, Norway, 1983.

40. Broek, David, Elementary Engineering Fracture Mechanics, 4th revised edition, Martinus Nijhoff Publishers, Boston, 1986.

41. Tipper, C.F., "*The Fracture of Metals*," Metallurgia, Vol.39, Jan 1949, pp.133-137.

42. Kardomateas, G.A. and McClintock, F.A., "*Tests and Interpretation of Mixed Mode I and II Fully Plastic Fracture from Simulated Weld Defects*," International Journal of Fracture, Vol.35, 1987, pp.103-124.

43. Hackett, E.M., Joyce, J.A. and Smith, C.F., "*Measurement of Dynamic Fracture Toughness of Ductile Metals*," DTNSRDC/SME-87-07, January 1987.

44. Atkins, A.G., "*Tearing of Thin Metal Structures*," presented at the International Symposium on Structural failure, Massachusetts Institute of Technology, Cambridge, Mass., 1988.

45. Mai, Y.M. and Cotterell, B., "*Effects of Pre-Strain on Plane Stress Ductile Fracture in  $\alpha$  - Brass*," Journal of Material Science, Vol.15, No.9, Sep 1980, pp.2296-2306.

46. Mai, Y.W. and Cotterell, B., "*The Essential Work of Fracture for Tearing of Ductile Metals*," International Journal of Fracture, Vol.24, 1984, pp.229-236.

47. Atkins, A.G., "*On the Number of Cracks in the Axial Splitting of Ductile Metal Tubes*," International Journal of Mechanical Science, Vol.29, 1987, pp.115-121.

48. U.S., Department of the Navy, Fitness for Service Analysis Addressing Linear Indications in CV-60 Class Main Propulsion Boilers, DTNSRDC/SME-85-96.



49. 1988 Annual Book of ASTM Standards, Vol.01.04, American Society for Testing and Materials, Easton, Md.,1988.

50. U.S., Department of the Navy, DDG-51 Longitudinal Strength Study, DWG 806-5774123.



## APPENDIX A

### Load Versus Displacement Experimental Data from Crushing of Test Specimens



BASE - 24 FEB , 29 APR 88

DEFLECTION (IN*1000)	LOAD (LBS)	DEFLECTION (IN*1000)	LOAD (LBS)
0	0	1203	4940
4	100	1251	4760
10	350	1292	4650
18	890	1331	4560
24	1760	1373	4400
27	2380	1394	4280 POPPING NOISE
31	3380	1440	4220
35	4670	1494	4120
39	5740	1546	3980
41	6550	1598	3940
44	7320	1634	3820
46	8040	1670	3750 POPPING NOISE
49	8840	1704	3680
51	9380	1751	3700
54	10170	1794	3700
56	10720	1851	3720
57	11060	1882	3780
58	11290	1921	3820
60	12120	1963	4150
62	12780	1981	4250
64	13280	2001	4290
64	13640	2039	4360
65	14240	2079	4380
66	14740	2122	4510
67	15310	2160	4600
68	15980	2192	4990
69	16400	2217	5110 POPPING NOISES
70	17160	2260	5380
73	18040	2284	5620
77	19160	2307	5790
80	20060	2327	5980
98	17020	2355	6270
102	16980	2382	6430
107	16300 PHOTO	2418	6730
122	15900	2439	6800
131	14800		
192	13180		
204	12860		
254	10940 PHOTO		
356	8290		
459	7220		
561	6620		
635	6240		
900	5420 LOST TRACKING		
998	5320		
1087	5060 PHOTO		
	CONTINUED TESTING		
1107	5100		
1126	5160		
1149	5090		
1172	5020		





A1 - 3, 29 FEB 88

DEFLECTION (IN*1000)	LOAD (LBS)	DEFLECTION (IN*1000)	LOAD (LBS)
0	20	234.5	8560
5.5	160	247	9220
18	1000	327	7800
26	1800	382	7050
31.5	2640	454	6240
36	3400	516.5	5900
40	4520	595	5450
43.5	5560	700	5440 EDGES FINCHING
46	6220	765	5800
49	7020		
53	8060		
58.5	9700		
66	10910		
73	11500		
78	11800		
83	12160		
97.5	12600		
105	12250		
108	12200		
114	12120		
120	11980		
124	11880		
132	11220		
134	11750		
136	11640		
141	11530		
145	11320		
153	11230		
157	11200		
160	11160		
167	10880		
175	10820		
180	10680		
180	10400		
187	10580		
194	10210		
196	10240		
201	10240		
212	8960		
217	8730		
221	8720		
227	9490		
228	9580		
246	9200		
248	8920		
249	8780		
250	9000		
255	8960		
	CONTINUED TESTING		
225	5640		
229	6920		
233	8200		



A2 - 16 FEB 88

DEFLECTION (IN*1000)	LOAD (LBS)	DEFLECTION (IN*1000)	LOAD (LBS)
0	0	1714	10165
3	60	1742.5	10180
11	440	1777	10380
16	1050	1824	10780
20.75	1880	1876	10990
29.5	4005	1920	11380
32.25	4560	1962	11480
36.75	5580	2009	11890
40	6360	2078	12210
42.75	7065	2144	12510
46	7840	2196	12820 PHOTO
49	8560	2279	12760 POPPING NOISES
52	9320	2290	12910
55	9930		LOST TRACKING
57	10330 PHOTO	2325	13050
61.25	10910	2340	13240
68	11400	2351	13200
96	11320	2368	13165 PHOTO-CLOSE UP
98.5	11320	2426	13600
101	11300	2448	13600
120	11100	2486	13800
128	10950	2551	13820 POPPING NOISES
146	10800	2603	13820
149.5	10640	2669	13620 POPPING NOISES
193	10230 PHOTO	2770	13480
207.75	9840		
273	8920		
399.25	8380		
509	6980		
613.5	5720		
728.75	4930 PHOTO		
	LOST TRACKING		
1380	8240		
1381	8600		
1383	7160		
1385	7640		
1402	8090		
1406	8420		
1416	8440		
1429	8480		
1440.5	8490		
1461	8610		
1481	8790		
1491	8840		
1522	9020		
1551	9120		
1573	9280		
1596	9520		
1626	9590		
1647	9650		
1686	9810		
1712	10040		



A3 - 14 MAR 88

DEFLECTION (IN*1000)	LOAD (LBS)	DEFLECTION (IN*1000)	LOAD (LBS)
0	0	1319	10280
5	10	1417	10680
8	20	1463	10700
15	20	1498	10800 PHOTO
25	20	1573	11120
30	20	1659	11490
35	20	1726	11580
40	90	1797	11980
45	270	1879	12360
56	2690	1951	12700
59	3720	2020	13120
63.5	5260		
68	6600		
72	7920		
75.5	8970		
78.5	9840		
81	10510		
85	11330		
89	12040		
91	12320		
97	12800		
116	12920		
115	12800		
145	12590 PHOTO		
175	12120		
222	11180		
256	10180		
302	9350		
351	8230		
402	7450		
506	6380		
547	6000		
614	5580 PHOTO		
694	5100		
766	4810		
801	5200		
805	5420		
818	5700		
833	6090		
896	6280 PHOTO		
867	6680		
919	7280		
979	7520		
982	7840		
1021	8290 NECKING AT CRACK TIP		
1041	8440		
1058	8610		
1082	8800		
1112	9090		
1148	9400		
1189	9720		
1282	10040		



B1 - 5 FEB, 26 APR 88

DEFLECTION (IN*1000)	LOAD (LBS)	DEFLECTION (IN*1000)	LOAD (LBS)
0	15		
7	180	202	9190
9.5	420	204.5	9100
12	720	212	8640 PHOTO
14	1130	223	8230
16	1440	230.5	7670
20	2370	234.25	7640
22	2800	254.5	7020
23	3200	273.5	6550
26	3900	308	5820
28	4380	323	5420
29	4860	429.5	4120
30	5325	456	3960
33	5970	516.5	3620
35	6360	536.5	3560
38	6950	615	3300
40.75	7450	725	3100
45	8150	823	3040
47	8600		CONTINUED TESTING
49	9160	845	3210
51.5	9650	855	3280
54.75	10205	884	3230
56	10455	911	3250
58.25	10810	955	3250
61	11210	1008	3240
64	11580	1042	3220
68	12020	1090	3200
70.75	12320	1146	3210
73	12440	1202	3260
74	12600	1232	3280
76	12760	1289	3290
77.5	12880	1317	3320
80	13060	1354	3340
82	13220	1414	3340
85	13465	1455	3390
89	13690 PHOTO	1490	3400
93	13850	1534	3440
95	14060	1599	3470
98	13920	1621	3520
99	13950	1658	3500
101	14020	1691	3550
103.5	14150	1721	3610
110	13680	1756	3610
112.25	13880	1791	3650
115	13780	1827	3710
117.5	13480	1871	3820
123	13560		
133	13720		
157	12180		
175	10800		
179	10620		
190.5	9920		





B2 - 16 FEB 88

DEFLECTION (IN*1000)	LOAD (LBS)
0	0
0.5	20
18.75	820
21	1420
23	2220
25	2940
26	3450
28.25	4460
30.75	5460
32.5	6220
35	7320
38	8460
41	9600
44.5	10910
46	11240
47	11610
48.75	11990
50.75	12450
51.75	12720
52.5	13020
53.75	13480
55	13700
56.5	13920
63.5	14310 PHOTO
75	14320
94.75	14010
102	13770
115	13220
171	10240
199	8720
277	5980
312.5	5150
353.75	4620
411	4030 PHOTO
500	3420
625.5	3250
719	3050
816	2970

DEFLECTION (IN*1000)	LOAD (LBS)
-------------------------	---------------



B3 - 14 MAR, 26 APR 88

DEFLECTION (IN*1000)	LOAD (LBS)	DEFLECTION (IN*1000)	LOAD (LBS)
0	0	1006	2780
7	20	1032	2790
12	20	1088	2790
21	20	1139	2800
31	240	1186	2850
35	1080	1259	2850
38.5	2170	1302	2910
43.5	3860	1335	2960
47	5280	1380	3010
48.75	5950	1420	3080
50.25	6600	1478	3130
52	7260	1543	3150
54	8080	1591	3170
55.5	8530	1646	3220
57	9080	1706	3230
58	9500	1732	3280
60	10090	1777	3380
62.5	10640	1829	3520
66.5	11390	1851	3560
67.5	11560	1901	3690
71	11960	1942	3720
74	12190	1984	3880
83	12550	2030	3980
94	12680	2077	4060
106	12680		
126	12440		
175	10640		
197	9880		
213	9300		
226	8580 PHOTO		
252	7790		
278	6250		
304	5380		
338	4700		
441	3680		
459	3600		
511	3390		
550	3160		
582	3130 PHOTO		
621	3050		
648	3000		
667	2970		
712	2860 PHOTO		
	CONTINUED TESTING		
732	2960		
756	2950		
782	2910		
822	2820		
850	2780		
887	2770		
943	2740		
986	2740		

















Thesis

S8641 Surko

c.1 The residual strength  
of a ship after an internal explosion.

Thesis

S8641 Surko

c.1 The residual strength  
of a ship after an internal explosion.



thesS8641

The residual strength of a ship after an



3 2768 000 79182 6

DUDLEY KNOX LIBRARY